A flexible workflow for simulating transcranial electric stimulation in healthy and lesioned brains

3   Benjamin Kalloch[1,2,*], Pierre-Louis Bazin[1,3], Arno Villringer[1], Bernhard Sehm[1], Mario Hlawitschka[1,2]

4

5

6   [1] Max Planck Institute for Human Cognitive and Brain Sciences, Leipzig, Germany

7   [2] Leipzig University of Applied Science, Leipzig, Germany

8   [3] University of Amsterdam, Amsterdam, The Netherlands

9

10   *Corresponding author

11   E-Mail: kalloch@cbs.mpg.de

1

Abstract

Simulating transcranial electric stimulation is actively researched as knowledge about the distribution of the electrical field is decisive for understanding the variability in the elicited stimulation effect. Several software pipelines comprehensively solve this task in an automated manner for standard use-cases. However, simulations for non-standard applications such as uncommon electrode shapes or the creation of head models from non-optimized T1-weighted imaging data and the inclusion of irregular structures are more difficult to accomplish.

We address these limitations and suggest a comprehensive workflow to simulate transcranial electric stimulation based on open-source tools. The workflow covers the head model creation from MRI data, the electrode modeling, the modeling of anisotropic conductivity behavior of the white matter, the numerical simulation and visualization.

Skin, skull, air cavities, cerebrospinal fluid, white matter, and gray matter are segmented semi-automatically from T1-weighted MR images. Electrodes of arbitrary number and shape can be modeled. The meshing of the head model is implemented in a way to preserve feature edges of the electrodes and is free of topological restrictions of the considered structures of the head model. White matter anisotropy can be computed from diffusion-tensor imaging data.

Our solver application was verified analytically and by contrasting tDCS simulation results with another simulation pipeline (SimNIBS 3.0). An agreement in both cases underlines the validity of our workflow.

Our suggested solutions facilitate investigations of irregular structures in patients (e.g. lesions, implants) or of new electrode types. For a coupled use of the described workflow, we provide documentation and disclose the full source code of the developed tools.

1. Introduction

The simulation of transcranial electric stimulation (tES) is increasingly employed when designing tES intervention studies (1) and observed behavior or neurophysiological changes are related to the simulated, subject-specific electric field (2), (3), (4). This development is motivated by increasing evidence that the individual distribution of the electrical field within each subject influences the stimulation effect (5), (6), (7). In addition, several software pipelines (8), (9), (10), (11), (12), among which SimNIBS (10) and ROAST (12) are currently most actively developed, make the simulation of tES more accessible to researchers.

All these pipelines implement a common, general workflow covering standard use cases, i.e. the tES simulation of healthy subjects based on their individual magnetic resonance imaging (MRI) data using rectangular or circular electrodes. The starting point of this workflow is the segmentation of the MRI data of the subjects into the electrically most important tissue classes. The obtained segmentation image is then used to create the head volume mesh, which is complemented by electrodes that need to be modeled and positioned. The simulation problem is solved using this individual head model, and results are visualized. The implementation of the outlined workflow by current tES simulation pipelines does not entirely cover use cases with suboptimal imaging data, the presence of pathological tissue in patients or alternative electrode shapes.

For instance, MRI data from large-scale imaging studies usually have not been primarily acquired for the purpose of computational head modeling. Performing simulation studies based on such data can become difficult due to challenges in the segmentation of low-contrast tissue such as skull using standard segmentation approaches. Following the image segmentation, a surface-based meshing approach is commonly used to create the head volume mesh. The advantage of this approach is a maximum of control over the approximation of the boundaries of the sub-compartments of the head model, which, on the other hand, must not intersect, restricting the topology of the included structures and complicating the inclusion of irregular tissue such as lesioned tissue. ROAST circumvents this

3

58   restriction by applying an image-based meshing approach, which is free of any topological constraints

59   (12), with the drawback of less accurate feature edges, for example of the electrodes. The shape of the

60   electrodes commonly can be selected from a set of standard shapes including rectangular, circular or

61   ring electrodes. Means for modeling non-standard shaped electrodes such triangular electrodes are

62   usually not provided. Finally, the visualization of the simulation results is typically realized in MATLAB

63   (8), (12), (11), GMSH (13) or a custom tool (9) and thus relatively limited.

64   In this work, we present approaches to address the above-mentioned non-standard use-cases when

65   simulating tES on an individual basis. Segmentation routines were selected based on the robustness of

66   the structure segmentation of T1-weighted MRI data using JIST (14) a plugin of MIPAV (15) to benefit

67   from a wide range of image manipulation and segmentation algorithms. We introduce an extension to

68   the image-based meshing approach presented in (12) by combining it with a surface-based meshing

69   approach for an accurate electrode representation. The 3D modeling software Blender (16) allows

70   highly flexible modeling of electrodes of arbitrary shapes. We suggest the use of ParaView (17) for a

71   versatile visualization of the simulation results. We describe the information flow among the involved

72   tools, which are arranged around OpenFOAM (18), a comprehensive, finite-volume-method-based

73   framework for the numerical simulations. The simulation was verified analytically and by contrasting

74   the numerical results with those of SimNIBS 3.0. A general agreement between both approaches

75   underlines the validity of our suggested solutions. The scripts and the custom source code along with

76   the documentation are readily available (from *https://gitlab.imn.htwk-leipzig.de/bkalloc1/tdcs-*

77   *pipeline.git*) allowing a coupled used of the entire toolset as well as usage of single tools only.

78

2. Methods

79

80 The process of simulating tES involves the head and the electrode modeling, solving the underlying

81 electrostatic problem, and the visualization.

82 The head model creation comprises the segmentation of the head MR image and the subsequent

83 volume mesh generation. Here, image segmentation is performed using the Java Image Science Toolkit

84 (JIST) (14) a plugin of the Medical Image Processing, Analysis, and Visualization (MIPAV) toolbox (15).

85 The volume mesh is generated using a combined image- and surface-based meshing approach

86 implemented as a custom application that uses the *Computational Geometry Algorithms Library* (CGAL)

87 API, version 4.13.1 (19). A plugin for the 3D modeling software Blender 2.79 (16) implements the

88 modeling and positioning of the electrodes. OpenFOAM 7.0 (18) provides the tools to define the

89 conductivity values of the mesh compartments. Additionally, information from diffusion-weighted

90 imaging (DWI) data can be incorporated to model the anisotropic conducting behavior of white matter

91 tissue, and are processed in MRTrix 3 (20). A plugin developed for the visualization software ParaView

92 5.6 (21) manages the calculation of the conductivity tensors derived from the diffusion tensors. The

93 finite volume calculations involved in solving the underlying Maxwell's equation are performed by a

94 custom solver application implementing the OpenFOAM API. Finally, the resulting electric field may be

95 visualized in ParaView. Fig. 1 illustrates the entire workflow.

96 **Fig 1, Data- and workflow.** *Schematics depicting the dataflow between the individual processing*

97 *steps and the involved tools as well as the expected input and output data of the individual stages.*

5

2.1 Set-up of the volume conductor model

2.1.1 MRI head segmentation

Accurate segmentation of the MR image is crucial since the segmented structures represent the individual compartments of the volume conductor model. Segmentation errors - especially discontinuities of the segmented skull or cerebrospinal fluid (CSF) - impair the simulation results (22). In our approach, we segment the scalp, the skull, the air-filled sinuses of the skull, the subarachnoid CSF, the CSF in the ventricles, the gray matter (GM) and the white matter (WM) only from T1-weighted MRI data. The involved segmentation process is described in our previous work (23). In short, we rely on robust, atlas-based segmentation techniques and image-processing capabilities implemented in JIST, a plugin of MIPAV. The segmentation of the scalp and skull structure of the image is achieved through the *Simultaneous Truth And Performance Level Estimation* algorithm (24). The intracranial compartments are segmented using the topology-preserving segmentation algorithm *Multi-object Geometric Deformable Model* (25) and the gyrification of the segmented GM surface is enhanced by the *Cortical Reconstruction Using Implicit Surface Evolution* method (26). We use a pseudo-CT template (27) to segment the air cavities in the skull. The quality of the generated segmentation images is improved by morphological image operations. The individual segmentation images are combined to a single image that contains a distinct, unique numeric label per segmented structure and is exported in the ANALYZE file format.

2.1.2 Electrode modeling and positioning

In our workflow a complete electrode model is implemented, which defines the electrodes geometrically in shape and position as well as their physical conductivity and the applied current, thereby realistically modeling the current shunt (28). The power source is represented by equipotential surfaces at the outer boundaries of the electrode. An optional gel layer may be modeled.

A custom Blender plugin geometrically models rectangular electrodes and positions them according to the international 10-20 system in a semi-automatic way. Necessary inputs are 1) a geometrical

6

123   representation of the outer boundary of the scalp segmentation in the Stereolithography (STL) file

124   format, 2) the extents of the electrode and 3) its location in 10-20 coordinates. Furthermore, the user

125   must provide four fiducial points, namely the nasion, inion and the tragi of the ears, on the scalp

126   surface by interactively aligning two reference lines and selecting the corresponding points on these

127   lines. The user interface is shown in Fig. 2 A.

128   **Fig 2, Electrode Modeling. A)** *The user interface of our Blender plugin for electrode positioning and*

129   *modeling purposes. Necessary input parameters constitute the electrode dimensions, position*

130   *according to the 10-20 system, and a geometrical representation of the outer boundary of the scalp*

131   *segmentation in the STL file format. A stepwise workflow to define fiducial points (nasion, inion,*

132   *tragi of the ears) for the computation of the 10-20 coordinate grid on the individual head is provided*

133   *by the GUI. The rectangular cube is generated according to the defined dimension and position of*

134   *the electrode and will be used to create the electrode by the means of constructive solid geometry*

135   *(CSG).* **B)** *Result obtained with our plugin: a standard rectangular patch electrode located at C3. A*

136   *smooth representation of the skin is generated, and the electrode is extruded based on the result of*

137   *the CSG operation of the cube and this skin surface.* **C)** *A ring electrode shape created by a non-*

138   *standard workflow. The cube was replaced by a cylinder with a hole.* **D)** *Triangular electrode*

139   *obtained by a non-standard workflow. The cube was replaced by a triangular prism.*

140   To create the geometrical surface representation of the outer scalp boundary from the binary scalp

141   segmentation image the Marching Cubes-based (MC) "Contour Filter" in ParaView is used. In Blender,

142   the plugin initially performs a Laplacian smoothing of the input scalp surface to mitigate its relatively

143   coarse structure due to the MC algorithm. Then, the location of the 10-20 coordinates on the

144   smoothed scalp surface is computed using the user-defined fiducial points. The smooth scalp surface

145   is clipped by the means of constructive solid geometry (CSG) at the specified location with a cube of

146   the specified extent. The position of this cube may be manually varied if the location of the electrode

147   falls outside the standard 10/20 grid. An arbitrary shape of the electrode (see Figs. 2 B - D) can be

148   achieved by replacing that cube with a volume of the desired shape. The clipped surface patch is

7

149 extruded in 1 mm steps to the desired electrode thickness. This avoids long, thin triangles at the

150 sidewalls of the electrode representation which are unfavorable for the subsequent volume meshing.

151 To model a gel layer this process is executed twice, and the electrode representation is moved on top

152 of the gel layer. The geometry of the electrodes, the gel layer, and the smooth skin surface are

153 exported as STL files.

154 The CSG operation may result in small, unfavorably clipped triangles at the edges of the electrode and

155 the gel layer that impede the subsequent volume mesh generation. Therefore, their geometry must

156 be cleaned in *Meshlab* (29) by unifying duplicate vertices and applying the "*Quadratic Edge Collapse*

157 *Decimation*" simplification filter. The smoothed skin surface, the cleaned electrodes, and the gel layer

158 are converted to the Object File Format (OFF).

159 ### 2.1.3 Volume meshing

160 An unstructured tetrahedral mesh constitutes the computational domain, i.e. the head model. We

161 approach the task of generating this mesh by applying a combination of an image-based meshing and

162 a surface-based meshing algorithm, both relying on Delaunay triangulation that is implemented in the

163 *Computational Geometry Algorithms Library* (CGAL), version 4.13.1. The surface-based meshing is

164 applied to the electrodes and the scalp structure and can be further utilized for any following internal

165 structure that does not impede a strictly nested arrangement of the mesh compartments. Structures

166 that violate a nested arrangement, such as the ventricles or lesioned tissue, can be meshed using the

167 image-based algorithm. Apart from the electrodes, the head mesh can be generated purely by image-

168 based meshing, as well as it is possible to create it solely using the surface-based approach. Compared

169 to surface-based meshing approaches where the mesh is generated from intermediate surfaces that

170 describe the boundaries of the mesh and its individual sub-compartments, image-based approaches

171 create the volume mesh from a labeled image and determine the boundaries of structures of different

172 labels via a bisection algorithm. In our case, which combines image-based and surface-based meshing,

173 the resulting mesh includes sub-compartments for every label found in the image and for every input

174 surface.

8

175 We created a C++ tool based on the *mesh_hybrid_mesh_domain* example of the CGAL library. The tool

176 combines the CGAL domain classes *Labeled_image_mesh_domain_3* and

177 *Polyhedral_mesh_domain_with_features_3* into a single hybrid domain to simultaneously employ an

178 image-based meshing together with a feature-preserving, surface-based meshing. As input, the tool

179 requires an ANALYZE label image of the subject comprising only the structures, for which the image-

180 based meshing should be used, as well as the OFF surface descriptions of the electrodes, the scalp and

181 any structure, for which the surface-based meshing approach is favored. The feature edges of the

182 electrodes are only preserved if the scalp is provided as a surface too.

183 To create the boundary surfaces for the surface-based volume meshing, we suggest a three-stage

184 process. The initial boundary surface descriptions are generated from the segmentation label image

185 by employing the Contour filter in ParaView, which is based on the Marching-cubes algorithm. Second,

186 to take full advantage of the accurate preservation of boundaries of the surface-based meshing, the

187 coarse output surfaces of the Contour filter must be smoothed in Meshlab using the Taubin smoothing

188 algorithm ($\lambda = 0.5, \mu = -0.53, \#smoothing\ steps = 50$). The smoothed scalp surface as a result of

189 the electrode placement procedure does not require additional smoothing. Finally, the quality of the

190 smoothed surface meshes must be improved by clearing defects (e.g. self-intersecting triangles) using

191 the MeshFix tool (v.2.1) (30) and by employing a custom tool leveraging the isotropic remeshing

192 functionality of CGAL's *Polygon_mesh_processing* class.

193 To minimize the deviations from the boundaries of the labeled structures during the image-based

194 meshing a small tolerance parameter $(10^{-6} \cong 0.00044\ mm$ at 1 mm voxel size) for the bisection

195 algorithm is used. Following the initial mesh generation, four optimizations can be optionally enabled.

196 Two global optimizers (*Optimized Delaunay Triangulation smoother*, *Lloyd smoother*) minimize the

197 total mesh energy. Two local optimizers improve the dihedral angles of the worst cells in the mesh or

198 eliminate triangles with a poor radius-edge ratio, so-called slivers, respectively. For further information

199 on these four optimizers, please refer to the CGAL documentation

200   (https://doc.cgal.org/latest/Mesh_3/group__PkgMesh__3Functions.htm). We use the API of GMSH

201   v.4.3 (31) to export the resulting volume mesh to the GMSH file format version 2.

202   The generated mesh is subsequently converted to the OpenFOAM format and optimized for the later

203   computations using the OpenFOAM utilities *gmshToFoam, transformPoints,* and *renumberMesh*

204   (details in Fig.1).

205   2.1.4 Conductivity values

206   We use the OpenFOAM *setFields* tool to uniformly set a distinct isotropic tensor value for all elements

207   of each sub-compartment of the mesh. This value is computed as the product of the unitary matrix

208   and the corresponding scalar conductivity value:

209    $$\sigma_{Tissue} = \sigma_{Tissue} \cdot \begin{bmatrix} 1 & 0 & 0 \\ 0 & 1 & 0 \\ 0 & 0 & 1 \end{bmatrix}.$$

210   To incorporate anisotropic conductivity information of the white matter, we adopted the volume-

211   constraint method (32). This approach assumes a shared principal direction between a diffusion tensor

212   and its corresponding conductivity tensor but different eigenvalues representing a fixed anisotropy

213   ratio between the principal and auxiliary directions. The calculation of the eigenvalues is based on the

214   scalar conductivity value of the white matter σ_{WM}, an anisotropy ratio of 1:10 and must satisfy the

215   conditions 1) $\sigma_{WM}^2 = \sigma_{main} \cdot \sigma_{aux}$, 2) $\sigma_{aux} = \frac{\sigma_{main}}{10}$ to ensure that no unreasonable conductivity values

216   are estimated. The conductivity tensor is determined by the both-sided multiplication of the matrix *S*

217   of   the   eigenvectors   of   the   diffusion   tensor   and   a   diagonal   matrix

218    $\sigma_T = S \cdot diag(\sigma_{main}, \sigma_{aux}, \sigma_{aux}) \cdot S^T$.

219   The DWI data are preprocessed using MRtrix 3 (20). First, the signal to noise ratio of the DWI data is

220   improved (*dwidenoise* (33)*, (34)*). Subsequently, artifacts due to eddy currents and due to motion are

221   corrected (*dwipreproc* (35)*, (36)*). For skull-stripping, a binary mask of the intracranial tissue is

222   generated (*dwi2mask* (37)). Tensor estimation is realized through *dwi2tensor* (38)*.* The resulting tensor

223   image is used to compute the fractional anisotropy (FA) map (*tensor2metric* (39)*, (40)*). Both the FA

224   map as well as the tensor image are cleaned from possible NaN values using *fslmaths*. The FA map is

10

225 registered to the T1-weighted brain image of the subject linearly using FSL *FLIRT* (41), (42) and non-

226 linearly with FSL *FNIRT* (43), (36). The calculated transformations are utilized to co-register the

227 diffusion tensor image using the tool *vecreg* which preserves the relative orientation of the tensors

228 upon transformation. The computation of the conductivity tensors is implemented as a ParaView

229 plugin. They are subsequently transferred to the OpenFOAM mesh of the respective head model in

230 ParaView and finally exported in the OpenFOAM field format using another custom plugin. The field

231 values are transferred to the already prepared field of isotropic conductivity tensors, overwriting the

232 values of the white matter compartment.

233 2.1.5 Boundary conditions

234 A Dirichlet Boundary condition for the electrical potential of +/- 5 V is assigned to the outer boundaries

235 of the anode and cathode respectively, regardless of the desired current strength. During post-

236 processing, the electrical field strength magnitude is corrected according to the actual current density

237 integrated at the contact surfaces of both electrodes with the scalp. The outer boundaries of the

238 electrodes are, thus, modeled as equipotential surfaces. Since the surrounding air is not explicitly

239 modeled and virtually acts as an insulator, a zero gradient Neumann boundary condition is applied for

240 the electrical potential at the scalp surface.

241 2.2 Solving the electrostatic problem

242 The electrical field strength E and the field of the electrical current density J are computed according

243 to the quasi-static form of Maxwell's equations which provide a sufficient approximation for tDCS, tACS,

244 and tRNS (44). Their solution is derived by our solver application using the OpenFOAM API.

245 2.2.1 Quasi-static form of Maxwell's equations

246 The electrical potential field ϕ induced by the electrodes subject to the conductivity σ of the volume

247 conductor is described by Laplace's equation $\nabla(\sigma \cdot \nabla \cdot \phi) = 0$. E is obtained by the component-wise

248 partial derivation of ϕ, $E = -\nabla \cdot \phi$. A linear relationship between E and J by σ exists as $J = \sigma \cdot E$.

249 2.2.2   The solver application

250 Our solver application computes the electrical current density *J* and the electrical field strength *E* using

251 the finite-volume method (FVM).

252 First, ϕ is computed using a Gauss discretization scheme with linear interpolation for the Laplace

253 operator at a residual of 10^{-6}. The solution is iterated to correct for non-orthogonality in the mesh

254 until the residual of the whole solution falls below 10^{-5}. Next, the gradient field *E* of ϕ is determined

255 using the least-squares gradient scheme. *J* is the product of *E* and the electrical conductivity σ.

256 Finally, *E* and *J* are scaled by the ratio $s = \frac{I_{target}}{I_{measured}}$ of the user-defined input current strength I_{target} and

257 the actual current strength $I_{measured}$ as determined by the summation of the current density across the

258 surface area where the electrodes contact with the scalp surface.

259 2.3 Visualization

260 Post-processing is handled by ParaView for which OpenFOAM provides a plugin to read the results. All

261 figures relating to simulation results have been created in ParaView.

262 3   Results

263 We demonstrate a 3-step verification attempt of the proposed workflow. First, our solver application

264 was tested using an analytically verifiable, 3-layered sphere model (45). Second, we utilized two

265 reference head models, which were generated in SimNIBS 3.0, to conduct tDCS simulations in both,

266 OpenFOAM and SimNIBS to compare the results using identical head models. While other simulation

267 pipelines are equally valid for comparing purposes, we chose the SimNIBS pipeline because of the

268 availability of test datasets. Finally, both head models were reproduced from their original MR image,

269 respectively, using our modeling workflow and a tDCS simulation in OpenFOAM was performed. The

270 simulation result obtained using these custom head models were compared to the previous results.

271   In addition, we demonstrate the capability to model anisotropic conductivity, the modeling of

272   alternative electrode shapes, namely small circular electrodes that are used for Laplacian-tDCS, as well

273   as the inclusion of irregular structures, lesions of the white matter, into the head model.

3.1 Analytical test case: 3-layer sphere model

275   We implemented the analytical solution to the tES problem with point electrodes in a 3-layered sphere

276   according to (45), (46) in Python and contrasted the result with the numerical simulation results

277   obtained by our solver application. Table 1 provides an overview of the model parameters. Since the

278   analytical case assumes a point electrode, which cannot be modeled in OpenFOAM, we simulated a 2

279   mm smaller sphere in OpenFOAM and used the analytical values greater than the 85th percentile of

280   the boundary of this sphere as the Dirichlet boundary condition of the numerical simulation. The

281   spherical domain consisted of 15.1 M. tetrahedra.

	Layer 1 (Scalp)	Layer 2 (Skull)	Layer 3 (Brain)
Radii (mm)	92 (90 in the numerical simulation)	85	80
Conductivity (S/m)	0.465	0.01	0.33

Table 1, Parameters of the 3-layerd spherical head model.

286   We found an overall agreement in the distribution of the electrical potential between the analytical

287   (Fig. 3A) and numerical solution resulting in a normalized root-mean-square deviation of only 2.1%

288   across the entire domain. The norm of the numerically calculated electrical potential tends to decline

289   slightly stronger as compared to the analytically derived potential (Fig. 3B).

Fig 3, Analytical 3-layered sphere model. A) Center slice of the analytical result field, illustrating the distribution of the electrical potential between the two opposing point electrodes. B) Comparison of the electrical potential calculated analytically according to (45) (blue graph) with the numerical solution derived by OpenFOAM (red graph).

3.2 Comparison to SimNIBS

Our workflow was evaluated using the *Almi5* and *Ernie* test datasets from SimNIBS. Simulation results were compared to that of SimNIBS.

3.2.1 Comparison of the solver application using the same head model

We utilized SimNIBS 3.0 to create the head models of the two test data sets from their T1- and T2-weighted imaging data. Each head model included the tissues skin, skull, CSF, GM, and WM. Compartments representing air were treated as a perfect insulator and were thus not part of the computational domain. For each head model, we tested three electrode setups, a bihemispheric setup over the primary motor cortices of both hemispheres, referred to as the dual setup, (10-20 positions: C3 and C4), an anodal setup (10-20 positions: C3, right supraorbital close to Fp2) and an occipital setup (10-20 positions: Cz, Oz) (Fig. 4). In all cases, square-shaped electrodes with 25 cm² dimensions were modeled as a complete electrode model with equipotential surfaces at the outer boundaries. Isotropic conductivities were adopted from the SimNIBS GUI (Table 2). The input current strength was 2 mA.

Fig 4, Electrode configuration. *Display of the anodal, dual and occipital electrode configuration of both head models, Almi and Ernie, used for comparison with SimNIBS.*

Structure	*Skin*	*Skull*	*Cerebrospinal fluid*	*Grey matter*	*White matter*	*Electrode material*
Conductivity, $\frac{S}{m}$	0.465	0.01	1.654	0.275	0.126	1.0

Table 2 Scalar conductivity values. *The conductivity values of the different head model compartments used for tDCS simulations both in OpenFOAM and SimNIBS.*

Visual comparison of the computed electrical field strength to the field obtained by SimNIBS revealed a comparable field pattern with hotspots at the same locations across both head models and all electrode montages (Fig. 5). The magnitude of the electrical field within the gray matter mesh compartment was on average higher in our results across both models and all electrode montages (Table 3). See tables 4 & 5 and Figs. 6 – 9 for a more detailed overview of the relative difference in magnitude of the electrical field strength as well as the angle difference across all conditions. The

320 deviation in direction was more pronounced in the area of the gray matter mesh compartment

321 underneath the electrodes in all cases with a 99th percentile peak value in angle difference of 40.56° in

322 the occipital electrode configuration of the Almi test case. We contrasted the magnitude of the

323 electrical field along a sampling line between the respective electrode pair of each condition through

324 the entire head model (Figs. 10 & 11). This assessment confirmed that our simulation slightly

325 overestimates the magnitude of the electrical field in the intracranial compartments. Interestingly, this

326 trend reverses for skin and skull, where a small underestimation can be observed. No major difference

327 between head models and electrode conditions was noticeable. The simulation time was

328 approximately 4 minutes in all cases.

---

329 **Fig 5, Electrical field pattern.** *Comparison of distribution pattern of the electrical field strength in*

330 *both head models and all electrode montages between the OpenFOAM result and the SimNIBS*

331 *result. Areas above the 90th percentile of the electrical field strength are defined as hotspots and*

332 *marked in black.*

Head Model		Type	Anodal			Dual			Occipital		
			90th pctl.	95th pctl.	99th pctl.	90th pctl.	95th pctl.	99th pctl.	90th pctl.	95th pctl.	99th pctl.
Ernie	SN mesh	OF sim	.098	.116	.159	.1	.118	.16	.082	.096	.129
			Mean: .054 [SD: .033]			Mean: .056 [SD: .032]			Mean: 0.052 [SD: .023]		
		SN Sim	.079	.09	.115	.078	.089	.111	.069	.078	.098
			Mean: .046 [SD: .024]			Mean: .046 [SD: .022]			Mean: .045 [SD: .017]		
	Custom mesh	OF sim	.12	.135	.164	.121	.139	.17	.11	.123	.148
			Mean: .072 [SD: .036]			Mean: .0.73 [SD: .034]			Mean: .072 [SD: .027]		
Almi	SN mesh	OF sim	.112	.131	.168	.115	.134	.17	.095	.11	.136
			Mean: .061 [SD: .036]			Mean: .063 [SD: .035]			Mean: .059 [SD: .026]		
		SN sim	.099	.112	.137	.097	.11	.134	.086	.097	.118
			Mean: .056 [SD: .029]			Mean: .056 [SD: .028]			Mean: .055 [SD: .022]		
	Custom mesh	OF sim	.152	.174	.218	.17	.2	.252	.145	.163	.199
			Mean: .091 [SD: .044]			Mean: .096 [SD: .051]			Mean: .088 [SD: .04]		

333

334

335

336

337

Table 3 Comparison electrical field strength (SimNIBS [SN] vs. OpenFOAM [OF]). *Comparison of the 90th, 95th, 99th percentile as well as the average magnitude of the electrical field strength in V/m within the gray matter mesh compartment of the head model generated by SimNIBS ("SN mesh") and the head model generated using our head modeling pipeline ("custom mesh"). For the SN mesh, simulations in both SimNIBS and OpenFOAM have been performed. The custom mesh was only used in our simulation environment, not in SimNIBS.*

	Anodal			Dual			Occipital		
	90th pctl.	*95th pctl.*	*99th pctl.*	*90th pctl.*	*95th pctl.*	*99th pctl.*	*90th pctl.*	*95th pctl.*	*99th pctl.*
Ernie	29.85 %	35.8 %	55.4 %	32.81 %	38.28 %	55.8 %	30.32 %	35.8 %	51.47 %
	Mean: 16.23 % [*SD*: 12.95 %]			*Mean*: 18.44 % [*SD*: 14.87 %]			*Mean*: 16.31 % [*SD*: 12.32 %]		
Almi	26.91 %	34.89 %	66.21 %	28.2 %	34.49 %	63.29 %	20.63 %	25.34 %	35.22 %
	Mean: 13.71 % [*SD*: 14.37 %]			*Mean*: 14.9 % [*SD*: 15.31 %]			*Mean*: 10.39 % [*SD*: 7.52 %]		

Table 4 Absolute value of the relative difference of the electrical field strength (SimNIBS vs OpenFOAM). *Comparison (in percent, $\frac{SimNIBS - OpenFOAM}{SimNIBS} \cdot 100$) of the mean and peak percentile absolute value of the relative difference of the simulation results computed by SimNIBS and OpenFOAM within the gray matter compartment of the reference meshes.*

	Anodal			Dual			Occipital		
	90th pctl.	*95th pctl.*	*99th pctl.*	*90th pctl.*	*95th pctl.*	*99th pctl.*	*90th pctl.*	*95th pctl.*	*99th pctl.*
Ernie	21.55°	26.25°	36.34°	22.37°	27.36°	37.9°	22.81°	27.73°	37.76°
	Mean: 11.05° [*SD*: 7.75°]			*Mean*: 11.44° [*SD*: 8.06°]			*Mean*: 11.72° [*SD*: 8.1°]		
Almi	20.63°	25.35°	35.22°	21.4°	26.4°	36.83°	22.15°	27.45°	40.56°
	Mean: 10.39° [*SD*: 7.52°]			*Mean*: 10.81° [*SD*: 7.81°]			*Mean*: 11.31° [*SD*: 8.65°]		

Table 5 Angle difference of the electrical field strength (SimNIBS vs. OpenFOAM). *Comparison of the simulation results (in degrees, $\frac{acos\left(\frac{dot(E_{OF}, E_{SN})}{|E_{OF}| \cdot |E_{SN}|}\right)}{\pi} \cdot 180$) computed by SimNIBS and OpenFOAM within the gray matter compartment of the reference meshes.*

16

353 **Fig 6, Relative difference in the electrical field strength magnitude - Almi.** *Heatmap of the relative*

354 *difference in the magnitude of the electrical field strength between OpenFOAM and SimNIBS in all*

355 *three electrode configurations. A red color indicates a higher electrical field strength in the*

356 *OpenFOAM result whereas blue indicates a higher value in the SimNIBS result. Histograms depict*

357 *differences in percent of all tetrahedra within the gray matter mesh compartment.*

358 **Fig 7, Angle difference in the electrical field strength - Almi.** *Heatmap of the angle difference of*

359 *the electrical field strength between OpenFOAM and SimNIBS of all electrode configurations.*

360 *Histograms depict angle differences in degrees of all tetrahedra within the gray matter mesh*

361 *compartment.*

362 **Fig 8, Relative difference in electrical field strength magnitude - Ernie.** *Heatmap of the relative*

363 *difference in the magnitude of the electrical field strength between OpenFOAM and SimNIBS in all*

364 *three electrode configurations. A red color indicates a higher electrical field strength in the*

365 **Fig 9, Angle difference in electrical field strength - Ernie.** *Heatmap of the angle difference of the*

366 *electrical field strength between OpenFOAM and SimNIBS of all electrode configurations.*

367 *Histograms depict angle differences in degrees of all tetrahedra within the gray matter mesh*

368 *compartment.*

369 **Fig 10, Electrical field magnitude - Almi.** *Comparison of the magnitude of the electrical field*

370 *strength along a sampling line between both electrodes between OpenFOAM (green) and SimNIBS*

371 *(blue). A dashed line depicts the mesh regions with distinct conductivity values.*

372 **Fig 11, Electrical field magnitude - Ernie.** *Comparison of the magnitude of the electrical field*

373 *strength along a sampling line between both electrodes between OpenFOAM (green) and SimNIBS*

374 *(blue). A dashed line depicts the mesh regions with distinct conductivity values.*

375

376

17

377 ## 3.2.2 Full workflow verification

378 As a next step, we reproduced the Almi5 and Ernie head models from their original T1-weighted MR

379 data using our head modeling workflow. Their original MR data are available from SimNIBS.

380 Figure 12 displays the segmentation results achieved by our approach using only the T1-weighted

381 image in comparison to SimNIBS 3.0 using the CAT12 segmentation routines on both the T1-weighted

382 as well as the T2-weighted image of the exemplary data set "Ernie". The computed head models were

383 caudally more truncated. The Mesh quality (Table 6) was well suitable for OpenFOAM. The conductivity

384 values and the three electrode montages remained unchanged. Computation times for each head

385 model on an Intel Core i7 6700 workstation were approximately 6 hours (segmentation), 3 hours

386 (meshing), 100 seconds (simulation).

387 **Fig 12, Head segmentation.** *Comparison of our segmentation result **(C)** of the T1-weighted MR*

388 *image of the Ernie test dataset **(B)** with the SimNIBS segmentation **(A)** computed from the T1- and*

389 *T2-weighted imaging. The resulting electrical field of an anodal electrode configuration using a*

390 *head model generated from our segmentation is displayed in Panel **D**.*

	Almi (dual)		Ernie (dual)	
	SimNIBS version	**Our version**	**SimNIBS version**	**Our version**
#cells (in million)	4.1	5.2	4.8	5.5
#non-orthogonal faces	1090	239	2301	26
Max. non-orthogonality	93.43°	81.04°	89.72°	82.12°
Max. cell skewness	10.9	2.39	3.04	1.78

391

392 **Table 6 Mesh characteristics.** *Number of cells and mesh quality metrics of our version of the Almi*

393 *and Ernie head models as well as the version generated by SimNIBS. For the subsequent finite-*

394 *volume-method calculation decisive characteristics are the number of mesh elements (#cells), the*

395 *number of non-orthogonal faces, i.e. faces whose non-orthogonality is greater than 70°, the*

396 *maximum non-orthogonality and the maximum skewness of the mesh elements.*

397 The magnitude of the resulting electrical field strength was again compared to the previous results by

18

398   sampling along a sampling line between the respective electrodes through the head models. Across all

399   conditions, the mean and percentile-peak values of the electrical field strength in the gray matter mesh

400   compartment were slightly overestimated ("custom mesh" vs "SN mesh" in Table 3) while the field

401   distribution (Fig. 12D) remained comparable (Fig. 13 & 14).

402   **Fig 13, Simulation results custom mesh vs SimNIBS mesh - Ernie.** *Comparison of the magnitude of*

403   *the electrical field strength of the simulation conducted using our custom head model (purple) and*

404   *the SimNIBS generated head model (OpenFOAM result: green, SimNIBS result: blue).*

405   **Fig 14, Simulation results custom mesh vs SimNIBS mesh - Almi.** *Comparison of the magnitude of*

406   *the electrical field strength of the simulation conducted using our custom head model (purple) and*

407   *the SimNIBS generated head model (OpenFOAM result: green, SimNIBS result: blue).*

3.3. Extended capabilities

409   In this section, we demonstrate extended processing capabilities that can be combined with our

410   standard workflow. We included anisotropic conductivity of the white matter in the custom Almi5 test

411   case. Furthermore, we conducted a simulation using an alternative electrode model in the form of

412   small circle-like electrodes in a multi-electrode setup. Finally, we demonstrate the inclusion of lesioned

413   tissue in a head model.

3.3.1. Modeling anisotropic conductivity

415   To model the anisotropic conductivity of white matter, the conductivity tensors from the diffusion-

416   weighted imaging data of the Almi5 dataset were computed. In this process, we assumed a fixed ratio

417   of 1:10 between the main and the auxiliary directions of the tensor and a conductivity of $0.126\frac{S}{m}$ for

418   the white matter. We assigned the same isotropic conductivity values to the individual mesh

419   compartments as before except the white matter compartment to which we assigned the computed

420   conductivity tensors. Refer to Fig. 15 for a depiction of the conductivity profile of the data set. We

421   simulated the anodal electrode setup with two 5 cm x 5 cm patch-like electrodes placed over C3 and

422   supraorbital, close to Fp2. The input current strength was set to 2 mA. Additionally, to demonstrate

423 the image-based meshing capabilities of our meshing tool we generated the head model only using

424 image-based meshing (except for the electrodes and the scalp to ensure the feature-preservation of

425 the electrodes). The characteristics of the resulting mesh were as follows: 5.2 million tetrahedra, 239

426 non-orthogonal faces, maximum non-orthogonality of 81°, maximum skewness of 2.4.

427 **Fig 15, Conductivity tensors**. *Conductivity profile of the augmented Almi5 test case. Darker color*

428 *depicts higher conductivity. Conductivity tensors are visualized using spherical tensor glyphs. Their*

429 *size depicts the magnitude of the conductivity. The shape reflects the degree of anisotropy, from*

430 *isotropic (ball shape) to highly anisotropic (ellipsoidal, rod-like).*

431 We sampled the magnitude of the electrical field strength along a sampling line between both

432 electrodes through the head model and compared the magnitude of the anisotropic test case to a

433 version of the test case using scalar conductivity values only. The difference in the magnitude was

434 most noticeable in the intracranial compartments, where the changes in the magnitude (both in the

435 negative and positive direction) along the sampling line were generally higher in the anisotropic case

436 as compared to the isotropic case (Fig. 16A). Furthermore, the area underneath the electrodes

437 experienced higher differences both in the local field angle and field magnitude of the electrical field

438 (Fig. 16B & 16C). The mean angle difference between the isotropic and anisotropic case within the

439 gray matter mesh compartment was 9.4° (99th percentile: 33.1°) and the mean value of the relative

440 difference of the absolute field magnitude was 12.25 % (99th percentile: 29.16%).

441 **Fig 16, Anisotropic test case – comparison to isotropic test case**. *A) Comparison of the magnitude*

442 *of the electrical field strength along the sampling line (yellow) between the custom version of the*

443 *Alim5 head model with isotropic and anisotropic white matter conductivity. B) Relative difference*

444

445 3.3.2. Simulating multi-electrode tDCS

446 In this test case, we changed the electrode setup to a 4 x 1 multi-electrode tDCS setup with five circular

447 electrodes with a diameter of 5 mm. The anode was positioned approximately at C3. The four cathodes

448   were positioned in 10 cm distance from the anode in a square arrangement around the cathode. A

449   Dirichlet boundary condition of -5 V at the four cathodes and +5 V at the central anode was defined.

450   We set the input current strength to 2 mA. Again, the image-based meshing algorithm was used for

451   the head model generation (surface-based only for the scalp and the electrodes). The same isotropic

452   conductivity values as before were assigned.

453   The computation of the electrical field finished after 148 seconds. The resulting electrical field pattern

454   is much more focal (Figure 17) with only a negligible fraction of the inbound current reaching the

455   contralateral hemisphere as compared to the field induced by two large conventionally shaped

456   electrodes as simulated before. This is an expected observation for multi-electrode tDCS montages.

457   The average electric field strength across the cortex was reduced to 0.02 V/m. The 99th percentile peak

458   electric field strength was lowered to 0.161 V/m. A larger portion of the cortex that received non-

459   negligible field strength is covered by a field strength of the 99th percentile.

460   **Fig 17, Multi-electrode test case**. *Exemplary extension of the standard workflow by multi-electrode*

461   *tDCS. Five round electrodes with a diameter of 5 mm were positioned approximately at C3 and*

462   *resulted in a much more focal field distribution than achieved with conventional square-shaped,*

463   *patch electrodes.*

3.3.3 Inclusion of lesioned tissue

465   In this test case, we created a head model from the T1-weighted magnetization prepared rapid

466   gradient echo (MRAGE) and T2-weighted fluid-attenuated inversion recovery (FLAIR) imaging data of

467   a single subject from the local, large-scale, cross-sectional study of the Leipzig Research Centre for

468   Civilization Diseases (LIFE) (47). Imaging parameters used for the MPRAGE image were: flip angle 9°,

469   repetition time 2300 ms, inversion time 900 ms, echo time 2.98 ms, 1 mm isotropic resolution,

470   acquisition time 5.1 min. The parameters of the FLAIR image were: repetition time 5000 ms, inversion

471   time 1800 ms, echo time 395 ms, 1 mm isotropic resolution, acquisition time 7.02 min. The images

472   were acquired on a MAGNETOM Verio scanner (Siemens, Erlangen, Germany) with a 32-channel head

473   receive coil and a body transmit coil. The head model was generated by our robust standard

474   segmentation workflow using the T1-weighted imaging data. Additionally, we included white-matter

475   lesions into the head model that were segmented before using the T2-FLAIR data. Details of the white

476   matter lesion segmentation procedure, which relied on an adapted version of the lesion-TOADS

477   algorithm (48), can be found in (49). We employed image-based meshing for the lesioned tissue, the

478   ventricles and the air cavities of the skull, and applied the surface-based meshing to all other structures

479   (scalp, skull, CSF, GM, WM, electrodes).

480   To illustrate the robustness of our segmentation and meshing approach, we compared the generated

481   compartments of the head mesh between our approach, SimNIBS 3.0 and ROAST 2.7.1 (Fig. 18). Our

482   approach strongly smooths the scalp structure but maintains typical characteristics of the shape of the

483   scalp (Fig.18A). The skull is most robustly estimated by our approach, which, however, tends to

484   overestimate the thickness of the skull occipitally, along the superior sagittal sinus (Fig.19B), and

485   caudally. All three approaches yield a comparable gray matter compartment (Fig.18D). SimNIBS

486   creates the visually most complete white matter compartment (Fig. 18E). Note that we included the

487   white matter lesions as a separate compartment only in our head model (highlighted in orange) (Fig.

488   18E, Fig. 19A).

489

490   **Fig 18, Mesh compartments of the head model generated using imaging data of the LIFE study**

491   (47). *The T1-weighted imaging data (A) of a subject from the local, large-scale cross-sectional*

492   *imaging study, LIFE, were used to create the head model using our approach, SimNIBS 3.0 and*

493   *ROAST 2.7.1. Our approach yielded the most robust skull segmentation (C). The skin compartment*

494   *(B) is highly smoothed while maintaining the basic shape. The cerebrospinal fluid (D) and gray*

495   *matter (E) mesh compartments are comparable across all three approaches. We included white*

496   *matter lesions (F, orange), which were segmented from an additional T2-FLAIR image, into the white*

497   *matter compartment of our head model.*

498

22

Fig 19, Visualization of the white matter lesions and skull thickness. *The white matter lesions of a subject exhibiting a high lesion load are highlighted in orange (A). Our atlas-based approach for skull segmentation tends to overestimate the thickness of the skull occipitally, along the superior sagittal sinus (B).*

We conducted a tDCS simulation using the generated white matter lesion head model with the following parameters: a bihemispheric setup of quadratic 5 cm by 5 cm electrodes as before, a 2 mA input current strength, default conductivity values from Table 2 for the standard tissue and 0.05 S/m for the lesioned tissue, modeling a calcification of the tissue. We then simulated the test case again assigning the conductivity of healthy white matter to the lesioned tissue. Comparing both computed electrical fields reveals a local perturbation in the area of the lesions (Fig. 20).

Fig 20, Simulation results using a white matter lesion head model. From the individual MR-image of subject **(A)** with a high lesion load (Fazekas score: 3) we segmented the standard tissue (skin, skull, csf, gray matter, white matter, air) and the white matter lesions **(B)**. We simulated **(C)** a bihemispheric electrode setup with quadratic 5 cm x 5 cm electrodes and a low conductivity of 0.05 S/m for the lesioned tissue while all other tissues were set to their default values (Table 2). For comparison we simulated again with the conductivity of the lesioned tissue set to that of healthy white matter **(D)**. A local perturbation of the electrical field in the area of the lesions can be observed.

4 Discussion

We presented a set of approaches for an individualized simulation of transcranial electric stimulation. The entire workflow from segmentation, meshing, electrode modeling, simulation, and visualization is built around OpenFOAM, a finite-volume based framework for numerical simulations. A coupled use, as well as the use of single features, are equally possible. Essential features are: 1) Individual head models are created solely from T1-weighted MRI data. Despite the limited T1-contrast we robustly segment scalp, skull, subarachnoid CSF, the ventricles, GM, WM, and the air cavities in the skull, as

23

524   demonstrated using an exemplarily head image from a local, large-scale imaging study (47). 2)

525   Combining image-based meshing with the surface-based meshing preserves the feature edges of the

526   electrodes while avoiding any restrictions concerning the topology of tissue structures of the head

527   model. 3) Arbitrary electrode shapes can be modeled, and their positioning is standardized according

528   to the international 10-20 system. 4) Anisotropic tissue conductivity can be incorporated into the

529   simulation. We demonstrated an overall agreement with an analytical 3-layer sphere model and the

530   simulation results obtained by the simulation pipeline SimNIBS, especially when the simulations are

531   based on the same head model, allowing comparability of the simulation results across simulation

532   studies.

533   The combination of an image-based and a surface-based meshing algorithm realizes the head model

534   generation. The image-based meshing holds two advantages. First, there is no restriction concerning

535   the topology of the sub-compartments of the mesh. As the boundaries are determined directly from a

536   labeled image, there is no requirement of overlap-free boundaries of sub-compartments (50).

537   Therefore, the inclusion of structures that do not obey a strictly nested arrangement, for example,

538   tumorous or lesioned tissue or holes in the skull (12), is facilitated. Second, image-based meshing is

539   less sensitive to the quality of the input data which avoids extensive postprocessing of the

540   segmentation images. However, boundaries may be less accurately approximated which we mitigated

541   by setting a strict tolerance of the involved bisection algorithm. Surface-based meshing approximates

542   boundaries most accurately and can preserve feature edges, which is, therefore, beneficial for

543   representing any structure that does not require the flexibility of the image-based meshing, especially

544   for the electrodes. As a consequence of the combination of both approaches, a tetrahedral volume

545   mesh of high quality with maximum flexibility concerning the topology and maximum geometrical

546   accuracy is obtained.

547   Comparing the results of our solver application and the solver employed in SimNIBS using an identical

548   head model indicated an overall agreement in the global distribution and changes of the electrical field

549   strength. However, peak differences of up to 66.2 % and peak deviations in the local electrical field

24

550   direction of up to 40.6° were revealed in sparse locations close to the electrodes while on average the

551   differences with the gray matter mesh compartments remained relatively small (approximately 15%

552   difference in the field magnitude and 11° in local field direction). Since the volume mesh, the boundary

553   conditions, and the conductivity values for the individual mesh compartments were identical, we

554   conclude that differences arose due to the fundamentally different numerical approaches used for

555   solving Maxwell's equation (SimNIBS: finite-element method, OpenFOAM: finite-volume method).

556   We consider the finite-volume method implemented in OpenFOAM more sensitive to the quality of

557   the volume mesh than the finite-element method in SimNIBS. Only by applying a limited interpolation

558   scheme for the Laplacian term of the underlying equation of the electrical potential, the solution

559   converged slowly when solving the tES problem in the head models created by SimNIBS. This choice of

560   the discretization scheme resulted in a decreased convergence and thereby an increased solution time

561   of approximately 4 minutes as compared to 100 seconds using our mesh with an even higher number

562   of tetrahedra (SimNIBS mesh ≈ 4 M., our head model ≈ 5 M.). In addition, we partly attribute the

563   observed differences between the solutions of the FVM solver and the FEM solver to the chosen

564   numerical scheme. Most notably our volume meshed contained in the worst-case approximately 220

565   non-orthogonal cells whereas the SimNIBS volume meshes exhibited more than 1000 non-orthogonal

566   cells in the best case and had problematic cells with negative cell volume, high skew, wrong orientation

567   and a high aspect ratio as detected by the checkMesh utility of OpenFOAM. The higher mesh quality is

568   the result of an extensive mesh optimization phase in our meshing approach, which increases the time

569   for the volume meshing to up to 3 hours as compared to 5 minutes without optimization.

570   Deviations in the electrical field strength when simulating with our version of the Almi5 and Ernie head

571   models instead of the ready-to-use head model might originate from differences in the caudal extent

572   of the head model (51) and a different segmentation of the white matter and especially of the skull

573   (Fig. 9). While our approach for skull segmentation tends to overestimate the skull caudally and

574   occipitally, along the superior sagittal sinus, it slightly underestimates the thickness dorsally where the

575   electrodes are attached. The thinner skull in that region may yield an overall higher electrical field

25

576   magnitude (50). However, the general agreement in the change of the magnitude of the electrical field

577   strength indicates that our modeling workflow does not introduce unexpected alterations to the head

578   model.

579   The Blender plugin provides powerful means for the positioning and the modeling of the electrodes.

580   After manually defining four fiducial points (nasion, inion, tragi of the ears) electrodes are placed

581   automatically according to the 10-20 system. Any position outside the 10-20 system can be manually

582   defined by moving the electrode across the scalp surface. A standard rectangular electrode is

583   automatically modeled at the specified position. Other electrode types such as ring electrodes or

584   triangular electrodes as applied in (52) and (53) are respectively possible, but require an adaption of

585   the automated workflow.

586   Our solver application was verified using an analytical 3-layered sphere model and by comparison of

587   the simulation results with the established simulation pipeline SimNIBS. However, a verification of the

588   obtained simulation results with in-vivo recordings of the electrical field remains an open task.

589   Promising approaches are electrical current density measurements obtained by the means of magnetic

590   resonance electrical impedance tomography (54) or in-vivo recordings of the electrical potential by

591   intracranial electrodes. TDCS simulations have been validated using intracranial recordings of epilepsy

592   patients before (55), (56).

593   Since our workflow mainly focuses on addressing individual problems that we faced during the

594   simulation of tDCS, it only provides a loose framework for the coupling of the suggested tools. These

595   tools may, therefore, be easily interchanged by other tools or extended by new functionalities.

596   However, familiarization with the individual tools and knowledge about the information flow between

597   the tools (Fig. 1) is necessary to apply the workflow as a whole and potentially results in a higher initial

598   effort for the setup and application as compared to fully automatized pipelines (10) (12).

599   First simulation studies suggest that damaged brain tissue due to a stroke influences the field

600   distribution (57). Considering pathological tissue in the head model is, therefore, a vital extension to

601 apply tES simulations to stroke patients. The coupled tools and the image-based meshing of our

602 approach are prepared for this application as we demonstrated by the inclusion of white matter lesions

603 into the head model. However, a fully automated and reliable segmentation of these irregular

604 structures, especially stroke lesions, is still an open task for future research.

605 The advantageous properties of our suggested approaches for head and electrode modeling, as well

606 as segmentation, facilitate simulation studies investigating alternative electrode shapes or irregular

607 structures of the head model such as lesions and tumors in patients, implants, holes in the skull or

608 vascular tissue.

Acknowledgments

References

612
613

1. Wang H, Wang X, Jin J, Zhang W, Li Y, Liu Z, et al. Simultaneous stimulation using rTMS and tDCS produces the most effective modulation of motor cortical excitability in healthy subjects: A pilot study. Neuroscience letters. 2019; 694: 46-50.

2. Antonenko D, Thielscher A, Saturnino GB, Aydin S, Ittermann B, Grittner U, et al. Towards precise brain stimulation: Is electric field simulation related to neuromodulation? Brain stimulation. 2019.

3. Laakso I, Mikkonen M, Koyama S, Hirata A, Tanaka S. Can electric fields explain inter-individual variability in transcranial direct current stimulation of the motor cortex? Scientific reports. 2019; 9: 626.

4. Kim JH, Kim DW, Chang WH, Kim YH, Kim K, Im CH. Inconsistent outcomes of transcranial direct current stimulation may originate from anatomical differences among individuals: electric field simulation using individual MRI data. Neuroscience letters. 2014; 564: 6-10.

5. Nitsche MA, Paulus W. Sustained excitability elevations induced by transcranial DC motor cortex stimulation in humans. Neurology. 2001; 57: 1899-1901.

6. Bikson M, Truong DQ, Mourdoukoutas AP, Aboseria M, Khadka N, Adair D, et al. Modeling sequence and quasi-uniform assumption in computational neurostimulation. Progress in brain research. 2015; 222: 1-23.

7. Datta A, Baker JM, Bikson M, Fridriksson J. Individualized model predicts brain current flow during transcranial direct-current stimulation treatment in responsive stroke patient. Brain stimulation. 2011; 4: 169-174.

8. Vorwerk J, Magyari L, Ludewig J, Oostenveld R, Wolters C. The FieldTrip-SimBio pipeline for finite element EEG forward computations in MATLAB: Validation and application. In the International Conference on Basic and Clinical Multimodal Imaging; 2013.

9. Dannhauer M, Khan A, White D, Guler S, Frisby S, MacLeod RS, et al. Brainstimulator: A Flexible Extensible Software Tool for Modeling and Optimizing Transcranial Brain Stimulation. Brain Stimulation: Basic, Translational, and Clinical Research in Neuromodulation. 2017; 10: e12--e13.

10. Thielscher A, Antunes A, Saturnino GB. Field modeling for transcranial magnetic stimulation: A useful tool to understand the physiological effects of TMS? In Engineering in Medicine and Biology Society (EMBC), 2015 37th Annual International Conference of the IEEE; 2015. p. 222-225.

11. Lee C, Jung YJ, Lee SJ, Im CH. COMETS2: An advanced MATLAB toolbox for the numerical analysis of electric fields generated by transcranial direct current stimulation. Journal of Neuroscience Methods. 2017; 277: 56-62.

12. Huang Y, Datta A, Bikson M, Parra LC. Realistic vOlumetric-Approach to Simulate Transcranial Electric Stimulation--ROAST--a fully automated open-source pipeline. bioRxiv. 2017;: 217331.

13. Saturnino GB, Madsen KH, Thielscher A. Efficient Electric Field Simulations for Transcranial Brain Stimulation. bioRxiv. 2019;: 541409.

14. Lucas BC, Bogovic JA, Carass A, Bazin PL, Prince JL, Pham DL, et al. The Java Image Science Toolkit (JIST) for rapid prototyping and publishing of neuroimaging software. Neuroinformatics. 2010; 8: 5-17.

15. Mcauliffe M, Lalonde F, McGarry DP, Gandler W, Csaky K, Trus B. Medical Image Processing, Analysis & Visualization in Clinical Research. In Proceedings of the 14th IEEE Symposium on Computer-Based Medical Systems; 2001 Feb. p. 381-386.

16. Foundation B. Blender.; 2017 [last access: 23.10.2017, https://www.blender.org].

17. Ahrens J, Geveci B, Law C. Paraview: An end-user tool for large data visualization. The visualization handbook. 2005; 717.

18. Foundation. TO. OpenFOAM.; 2017 [last access: 23.10.2017, http://www.openfoam.org/].

19. Fabri A, Pion S. CGAL: The computational geometry algorithms library. In Proceedings of the 17th ACM SIGSPATIAL international conference on advances in geographic information systems; 2009. p. 538-539.

20. Tournier JD, Calamante F, Connelly A. MRtrix: diffusion tractography in crossing fiber regions. International Journal of Imaging Systems and Technology. 2012; 22: 53-66.

21. Ayachit U. The ParavView guide: Kitware; 2007.

22. Huang Y, Su Y, Rorden C, Dmochowski J, Datta A, Parra LC. An automated method for high-definition transcranial direct current stimulation modeling. In Engineering in Medicine and Biology Society (EMBC), 2012 Annual International Conference of the IEEE; 2012. p. 5376-5379.

23. Kalloch B, Bode J, Kozlov M, Pampel A, Hlawitschka M, Sehm B, et al. Semi-automated generation of individual computational models of the human head and torso from MR images. Magnetic resonance in medicine. 2018.

24. Warfield SK, Zou KH, Wells WM. Simultaneous truth and performance level estimation (STAPLE): an algorithm for the validation of image segmentation. Medical Imaging, IEEE Transactions on. 2004; 23: 903-921.

25. Bogovic JA, Prince JL, Bazin PL. A multiple object geometric deformable model for image segmentation. Computer Vision and Image Understanding. 2013; 117: 145-157.

26. Han X, Pham DL, Tosun D, Rettmann ME, Xu C, Prince JL. CRUISE: cortical reconstruction using implicit surface evolution. NeuroImage. 2004; 23: 997-1012.

27. Rorden C, Bonilha L, Fridriksson J, Bender B, Karnath HO. Age-specific CT and MRI templates for spatial normalization. Neuroimage. 2012; 61: 957-965.

28. Wagner S, Lucka F, Vorwerk J, Herrmann CS, Nolte G, Burger M, et al. Using reciprocity for relating the simulation of transcranial current stimulation to the EEG forward problem. Neuroimage. 2016; 140: 163-173.

29. Cignoni P, Callieri M, Corsini M, Dellepiane M, Ganovelli F, Ranzuglia G. MeshLab: an Open-Source Mesh Processing Tool. In Scarano V, Chiara RD, Erra U, editors. Eurographics Italian Chapter Conference; 2008: The Eurographics Association.

30. Attene M. A lightweight approach to repairing digitized polygon meshes. The visual computer. 2010; 26: 1393-1406.

31. Geuzaine C, Remacle JF. Gmsh: A 3-D finite element mesh generator with built-in pre-and post-processing facilities. International journal for numerical methods in engineering. 2009; 79: 1309-1331.

32. Wolters CH, Anwander A, Tricoche X, Weinstein D, Koch MA, MacLeod RS. Influence of tissue conductivity anisotropy on EEG/MEG field and return current computation in a realistic head model: a simulation and visualization study using high-resolution finite element modeling. NeuroImage. 2006; 30: 813-826.

33. Veraart J, Fieremans E, Novikov DS. Diffusion MRI noise mapping using random matrix theory. Magnetic resonance in medicine. 2016; 76: 1582-1593.

34. Veraart J, Novikov DS, Christiaens D, Ades-Aron B, Sijbers J, Fieremans E. Denoising of diffusion MRI using random matrix theory. NeuroImage. 2016; 142: 394-406.

35. Andersson JLR, Sotiropoulos SN. An integrated approach to correction for off-resonance effects and subject movement in diffusion MR imaging. Neuroimage. 2016; 125: 1063-1078.

36. Smith SM, Jenkinson M, Woolrich MW, Beckmann CF, Behrens TEJ, Johansen-Berg H, et al. Advances in functional and structural MR image analysis and implementation as FSL. Neuroimage. 2004; 23: S208--S219.

37. Dhollander T, Raffelt D, Connelly A. Unsupervised 3-tissue response function estimation from single-shell or multi-shell diffusion MR data without a co-registered T1 image. In ISMRM Workshop on Breaking the Barriers of Diffusion MRI; 2016.

38. Veraart J, Sijbers J, Sunaert S, Leemans A, Jeurissen B. Weighted linear least squares estimation of diffusion MRI parameters: strengths, limitations, and pitfalls. NeuroImage. 2013; 81: 335-346.

39. Basser PJ, Mattiello J, LeBihan D. MR diffusion tensor spectroscopy and imaging. Biophysical journal. 1994; 66: 259-267.

40. Westin CF, Peled S, Gudbjartsson H, Kikinis R, Jolesz FA. Geometrical Diffusion Measures for MRI from Tensor Basis Analysis. In ISMRM '97; 1997 Apr; Vancouver Canada. p. 1742.

41. Jenkinson M, Smith S. A global optimisation method for robust affine registration of brain images. Medical image analysis. 2001; 5: 143-156.

42. Jenkinson M, Bannister P, Brady M, Smith S. Improved optimization for the robust and accurate linear registration and motion correction of brain images. Neuroimage. 2002; 17: 825-841.

43. Andersson JLR, Jenkinson M, Smith S, others. Non-linear registration, aka Spatial normalisation FMRIB technical report TR07JA2. FMRIB Analysis Group of the University of Oxford. 2007; 2: 1-21.

44. Ruffini G, Wendling F, Merlet I, Molaee-Ardekani B, Mekonnen A, Salvador R, et al. Transcranial current brain stimulation (tCS): models and technologies. IEEE Transactions on Neural Systems and Rehabilitation Engineering. 2013; 21: 333-345.

45. Rush S, Driscoll DA. Current distribution in the brain from surface electrodes. Anesthesia & Analgesia. 1968; 47: 717-723.

46. Rush S, Driscoll DA. EEG electrode sensitivity-an application of reciprocity. IEEE transactions on biomedical engineering. 1969;: 15-22.

47. Loeffler M, Engel C, Ahnert P, Alfermann D, Arelin K, Baber R, et al. The LIFE-Adult-Study: objectives and design of a population-based cohort study with 10,000 deeply phenotyped adults in Germany. BMC public health. 2015; 15: 691.

48. Shiee N, Bazin PL, Ozturk A, Reich DS, Calabresi PA, Pham DL. A topology-preserving approach to the segmentation of brain images with multiple sclerosis lesions. NeuroImage. 2010; 49: 1524-1535.

49. Lampe L, Kharabian-Masouleh S, Kynast J, Arelin K, Steele CJ, Löffler M, et al. Lesion location matters: the relationships between white matter hyperintensities on cognition in the healthy elderly. Journal of Cerebral Blood Flow & Metabolism. 2019; 39: 36-43.

50. Nielsen JD, Madsen KH, Puonti O, Siebner HR, Bauer C, Madsen CG, et al. Automatic skull segmentation from MR images for realistic volume conductor models of the head: Assessment of the state-of-the-art. NeuroImage. 2018; 174: 587-598.

51. Indahlastari A, Chauhan M, Schwartz B, Sadleir RJ. Changing head model extent affects finite element predictions of transcranial direct current stimulation distributions. Journal of neural engineering. 2016; 13: 066006.

52. Sehm B, Hoff M, Gundlach C, Taubert M, Conde V, Villringer A, et al. A novel ring electrode setup for the recording of somatosensory evoked potentials during transcranial direct current stimulation (tDCS). Journal of neuroscience methods. 2013; 212: 234-236.

53. Riedel P, Ragert P, Schelinski S, Kiebel SJ, Kriegstein K. Visual face-movement sensitive cortex is relevant for auditory-only speech recognition. Cortex. 2015; 68: 86-99.

54. Kasinadhuni AK, Indahlastari A, Chauhan M, Schär M, Mareci TH, Sadleir RJ. Imaging of current flow in the human head during transcranial electrical therapy. Brain stimulation. 2017; 10: 764-772.

55. Huang Y, Liu AA, Lafon B, Friedman D, Dayan M, Wang X, et al. Measurements and models of electric fields in the in vivo human brain during transcranial electric stimulation. eLife. 2017; 6: e18834.

56. Opitz A, Falchier A, Yan CG, Yeagle EM, Linn GS, Megevand P, et al. Spatiotemporal structure of intracranial electric fields induced by transcranial electric stimulation in humans and nonhuman primates. Scientific reports. 2016; 6: 31236.

57. Minjoli S, Saturnino GB, Blicher JU, Stagg CJ, Siebner HR, Antunes A, et al. The impact of large structural brain changes in chronic stroke patients on the electric field caused by transcranial brain stimulation. NeuroImage: Clinical. 2017; 15: 106-117.
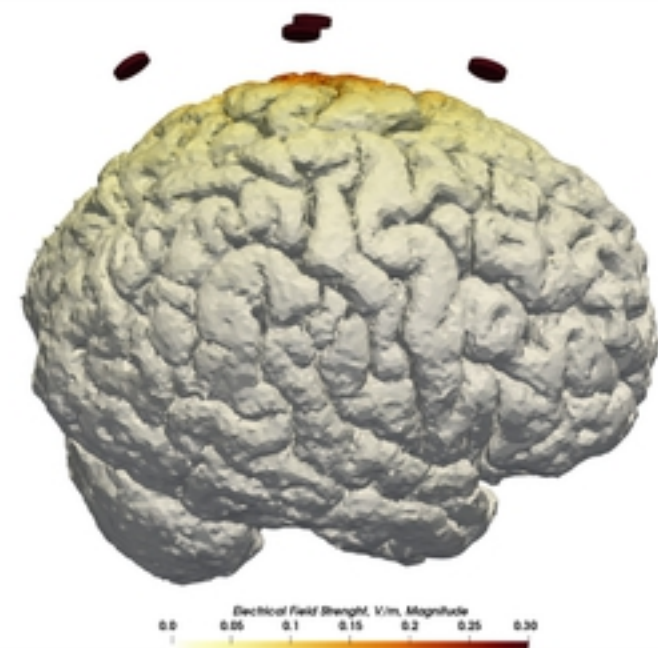
Figure 1

Figure 2

A

B Three-concentric spheres analytical model

— OpenFOAM, ElPot
— RushDriscoll, ElPot

Z Axis

Y Axis

Electrical Potential, Volts

−0.00018   0   0.00018

Electrical potential, Volts

Arc length
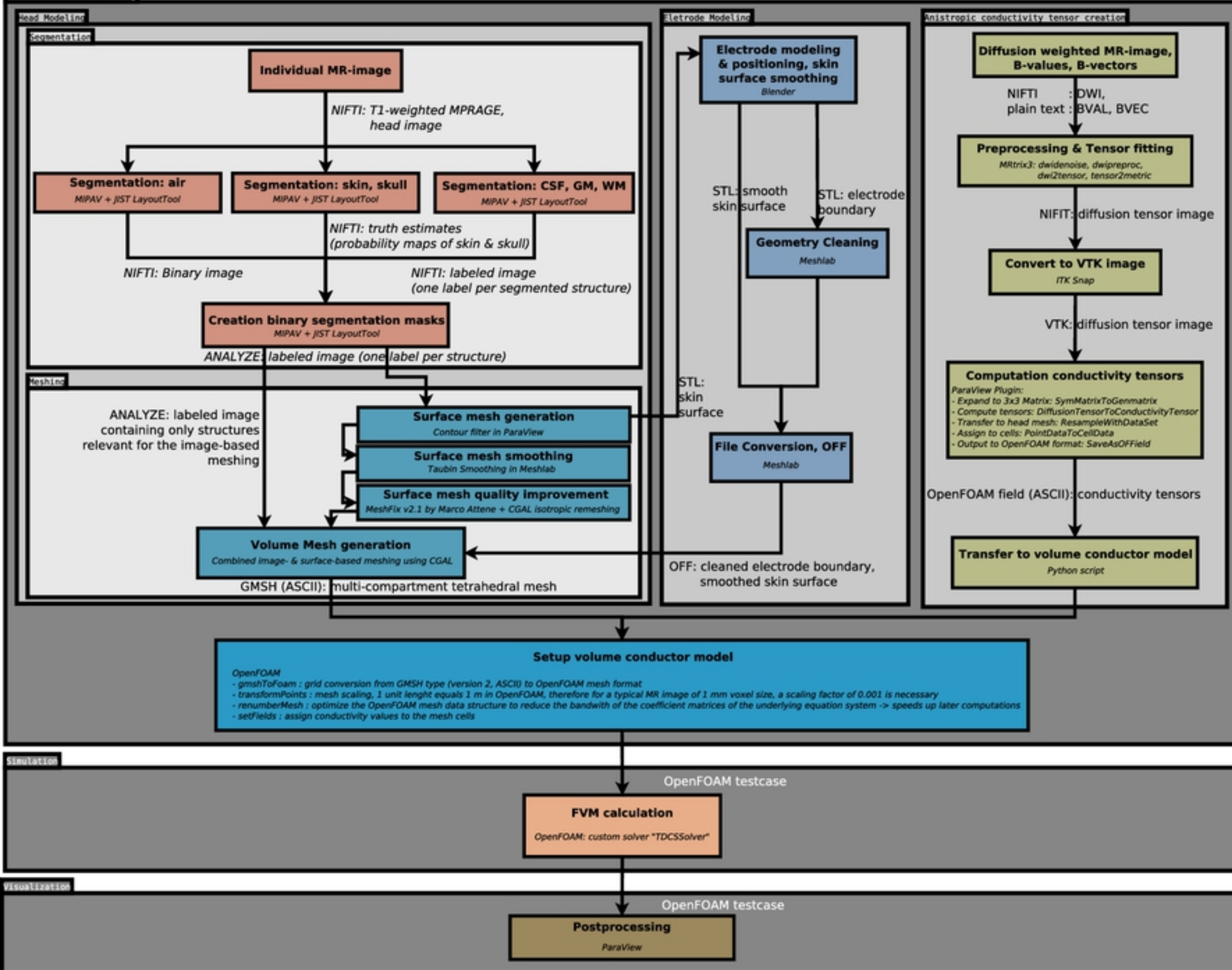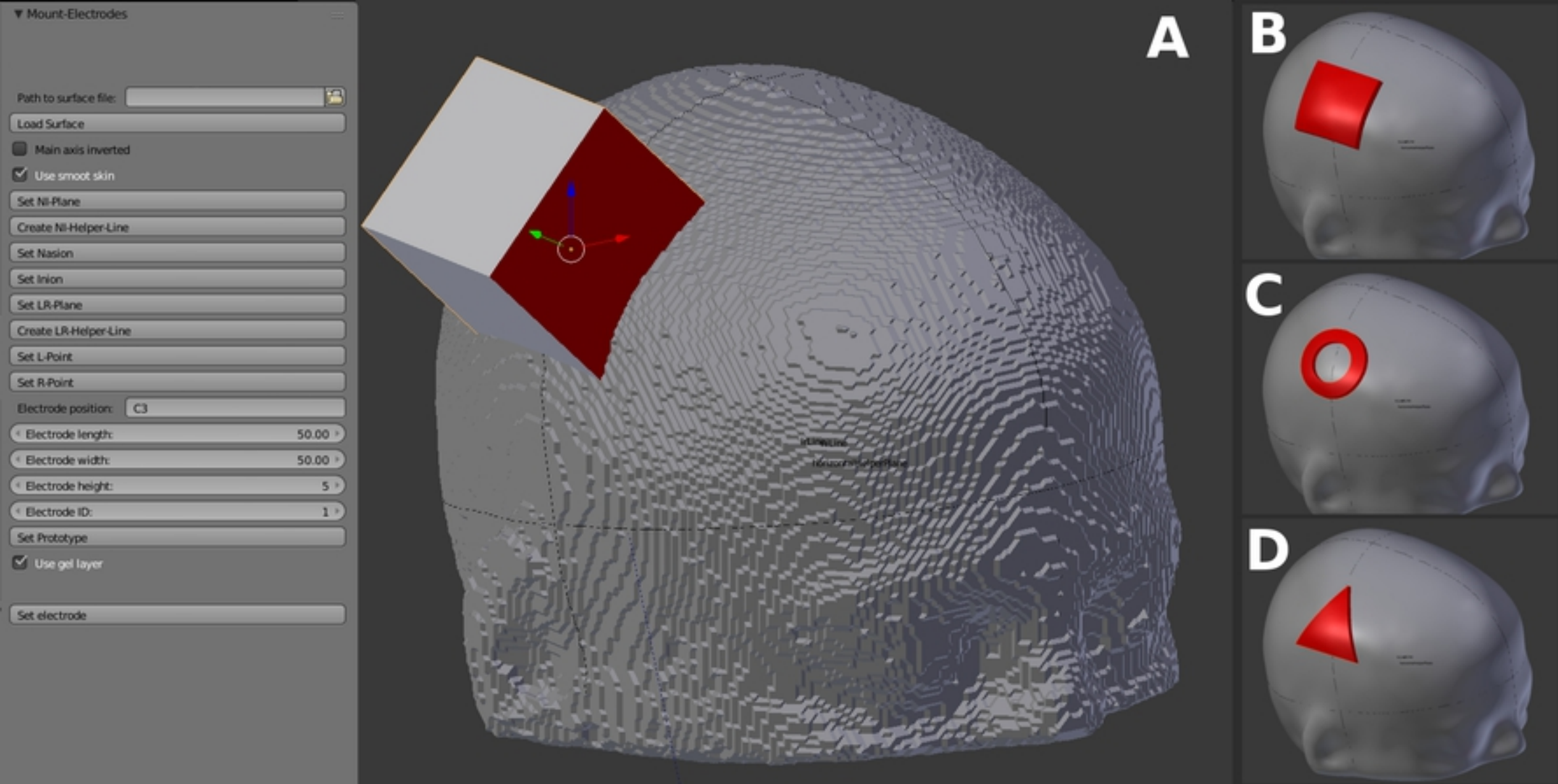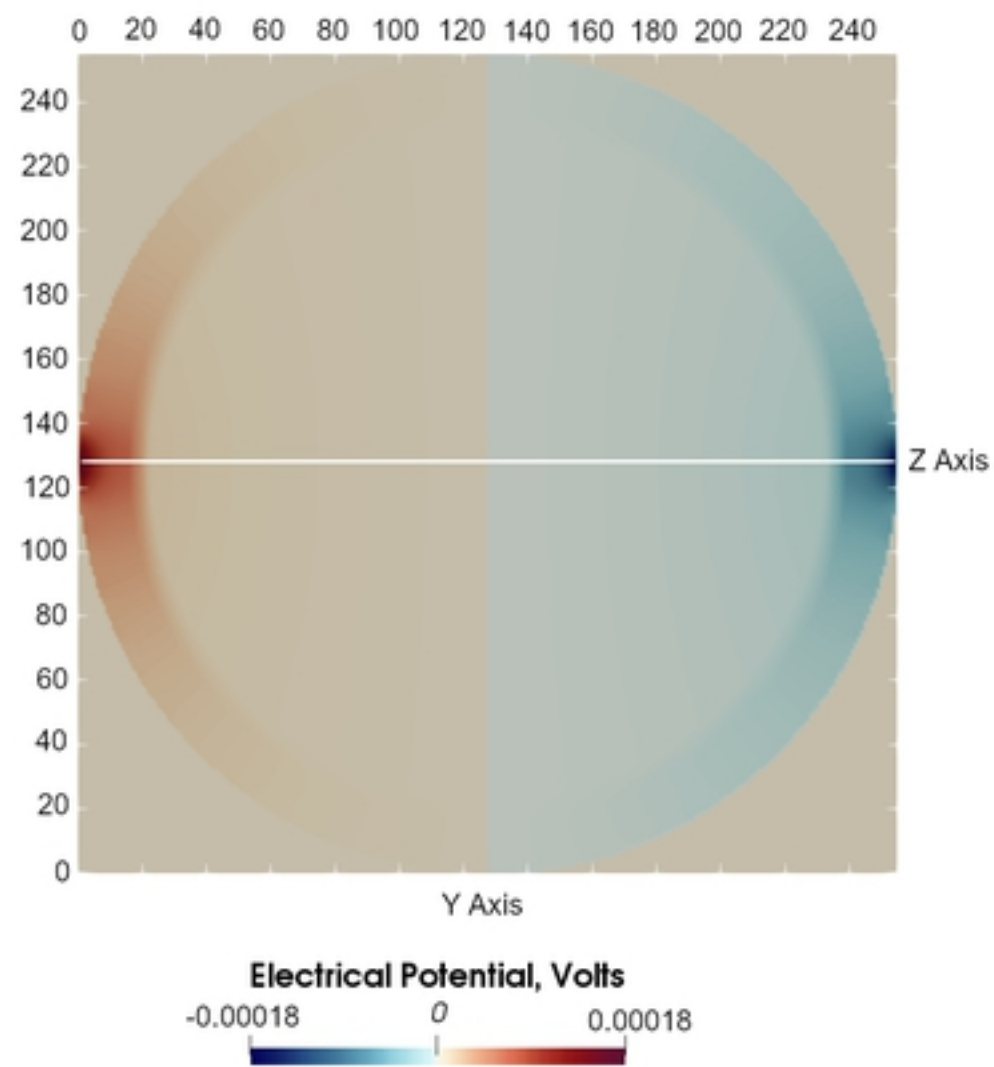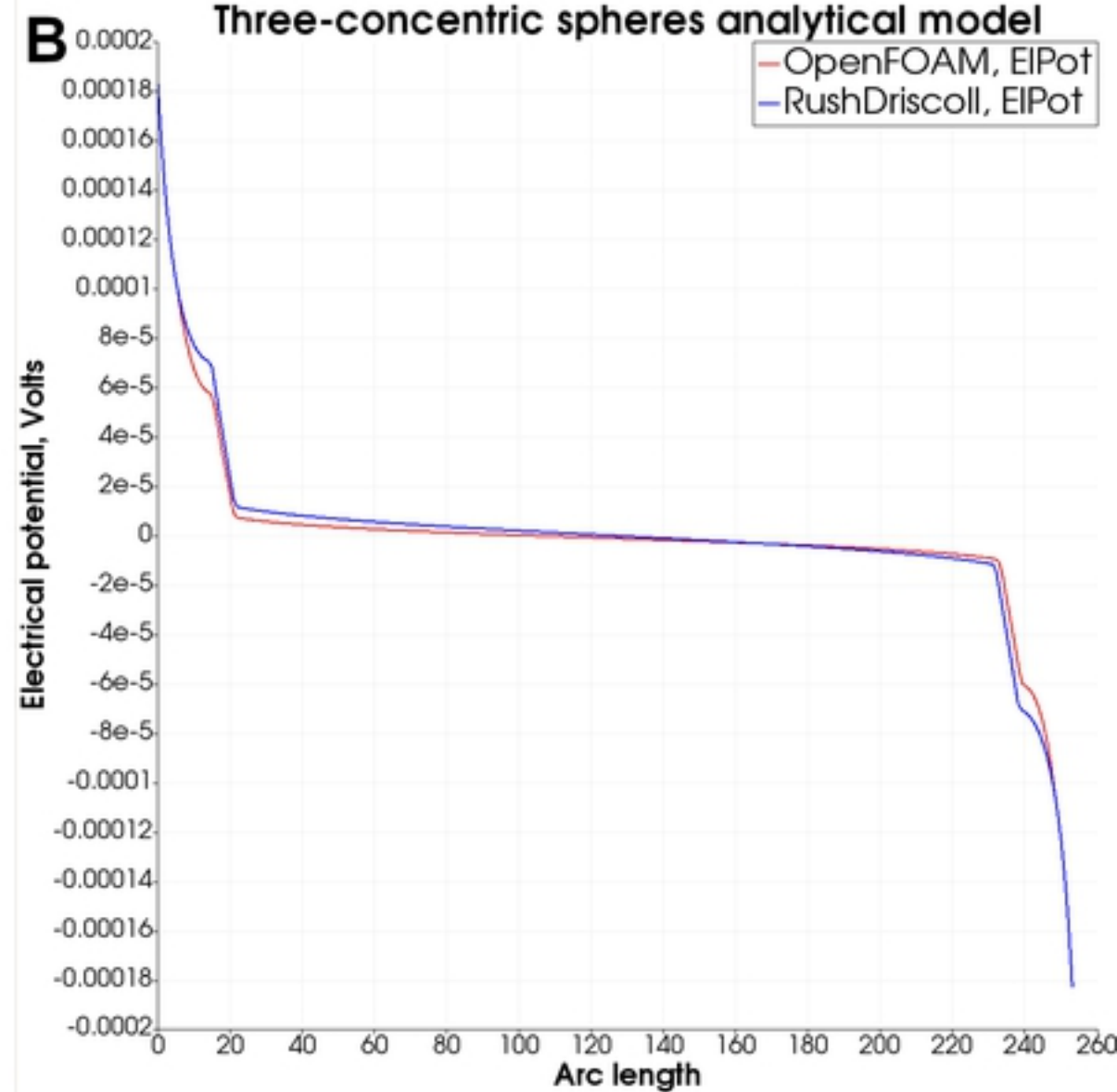
Figure 3

	Anodal	**Dual**	**Occipital**

Almi
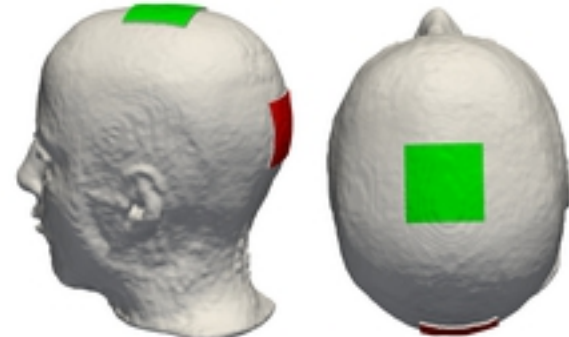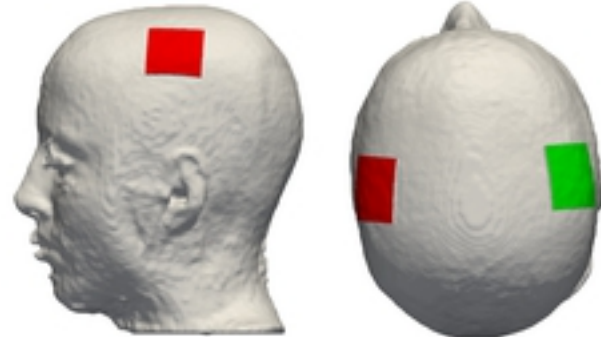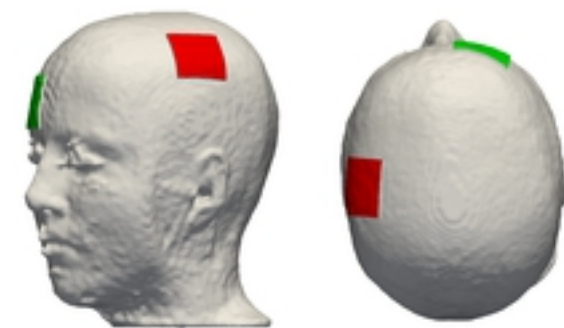
Ernie
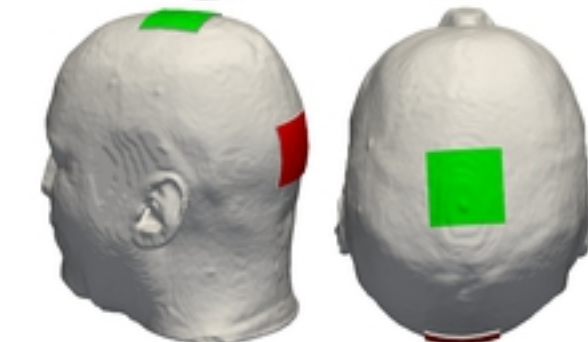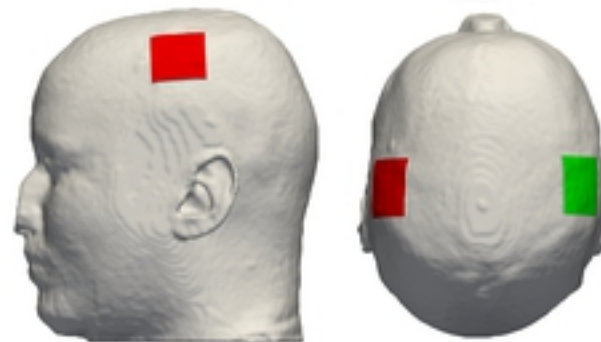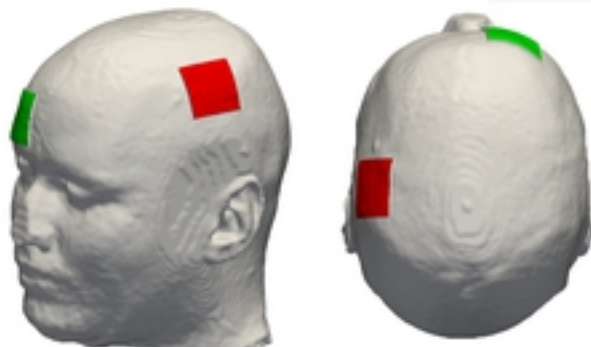
Figure 4
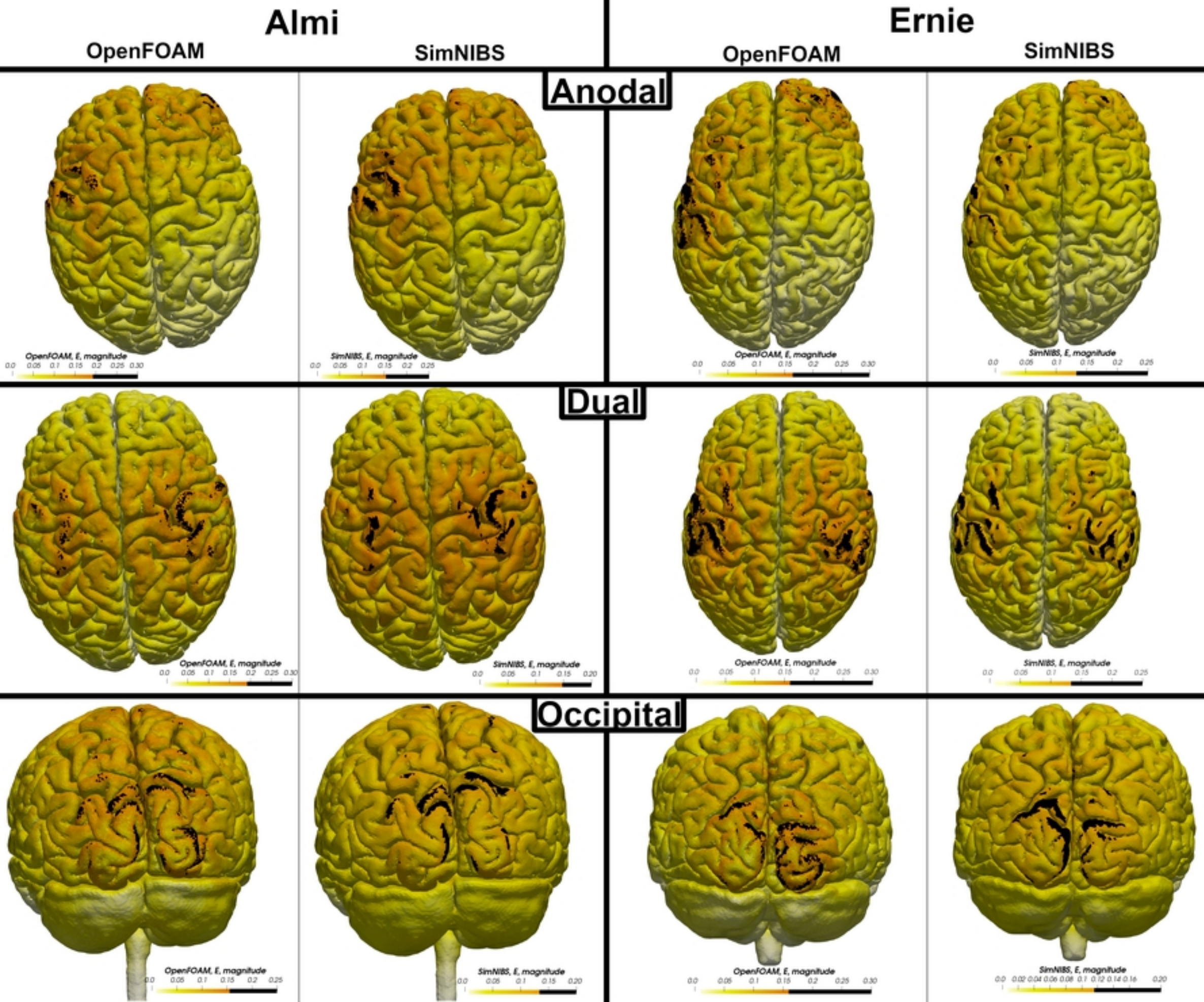
Figure 5
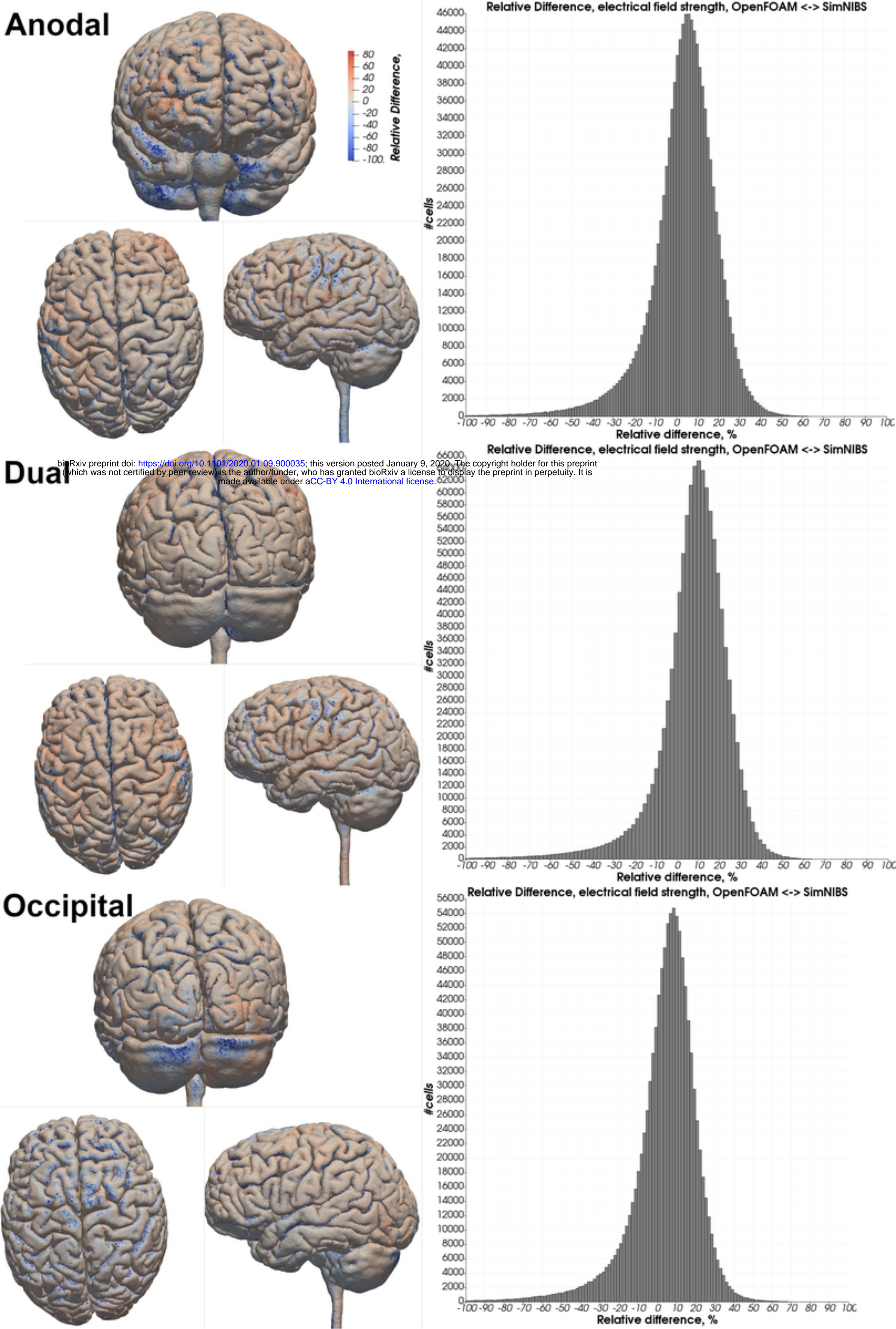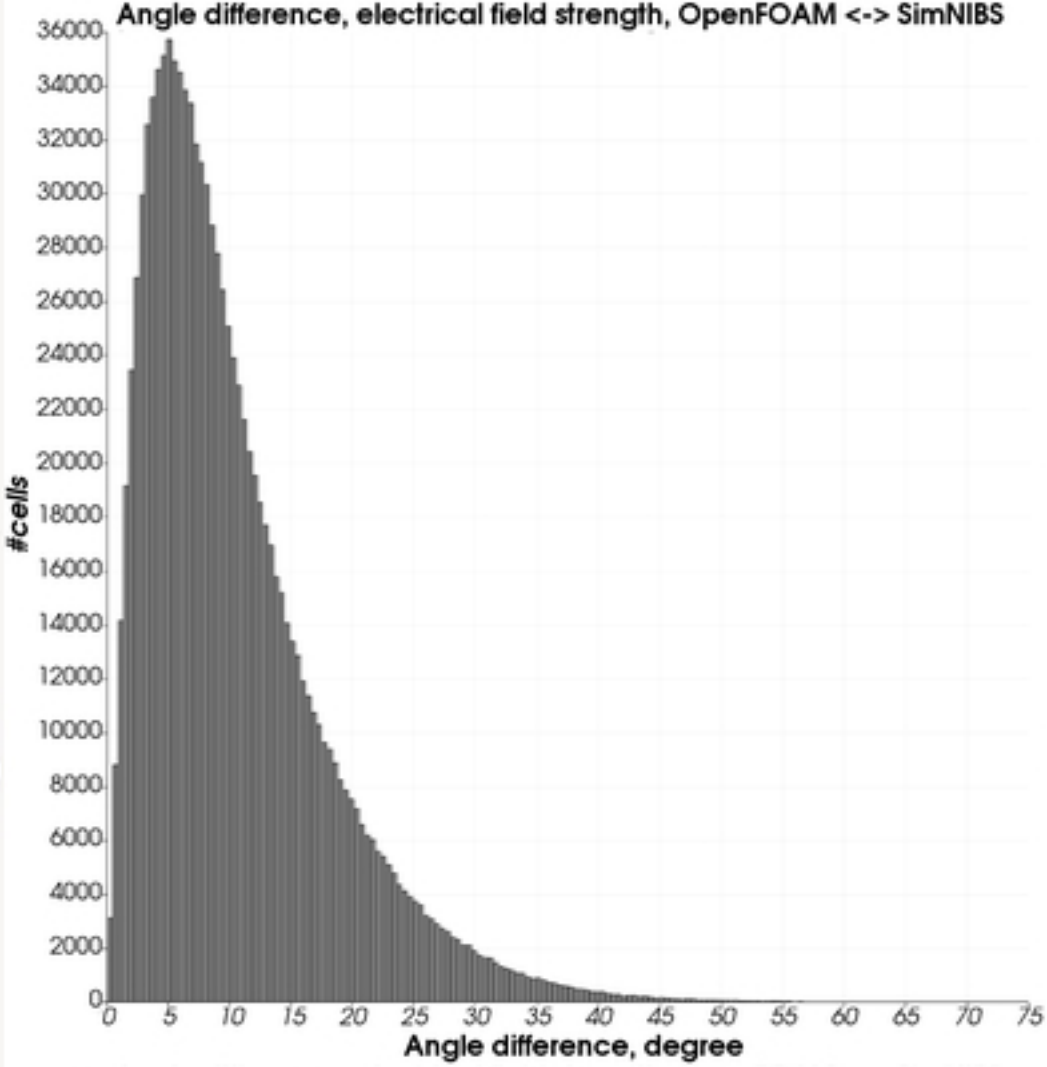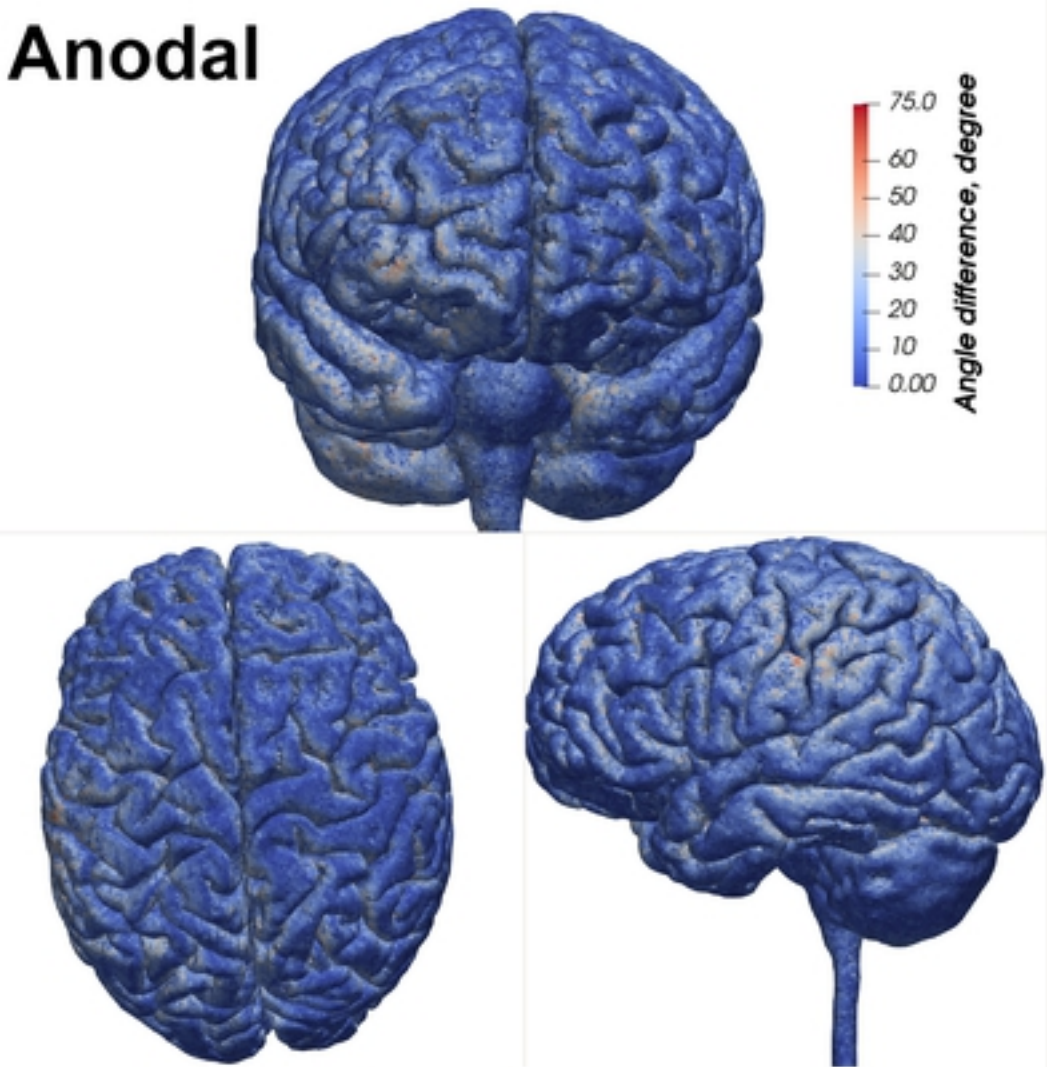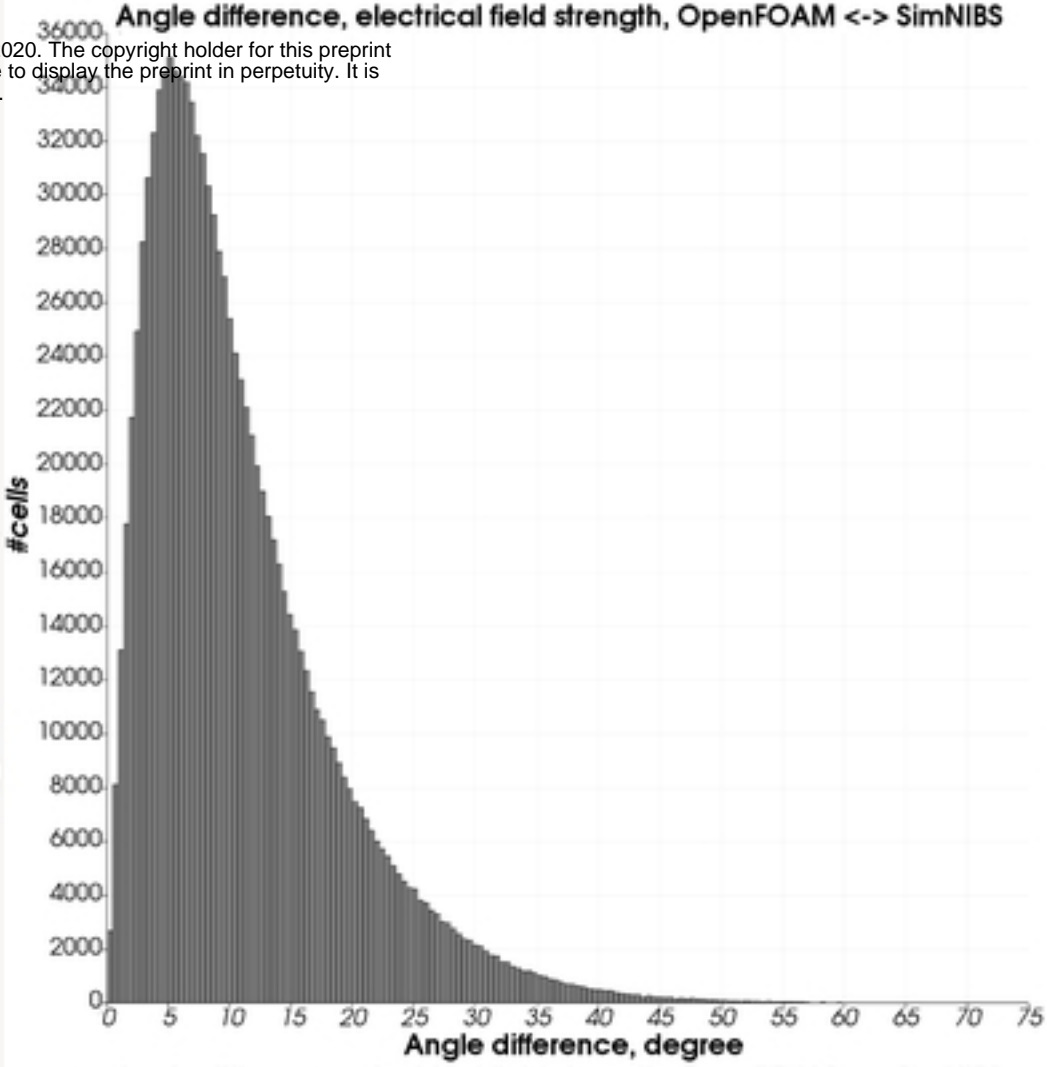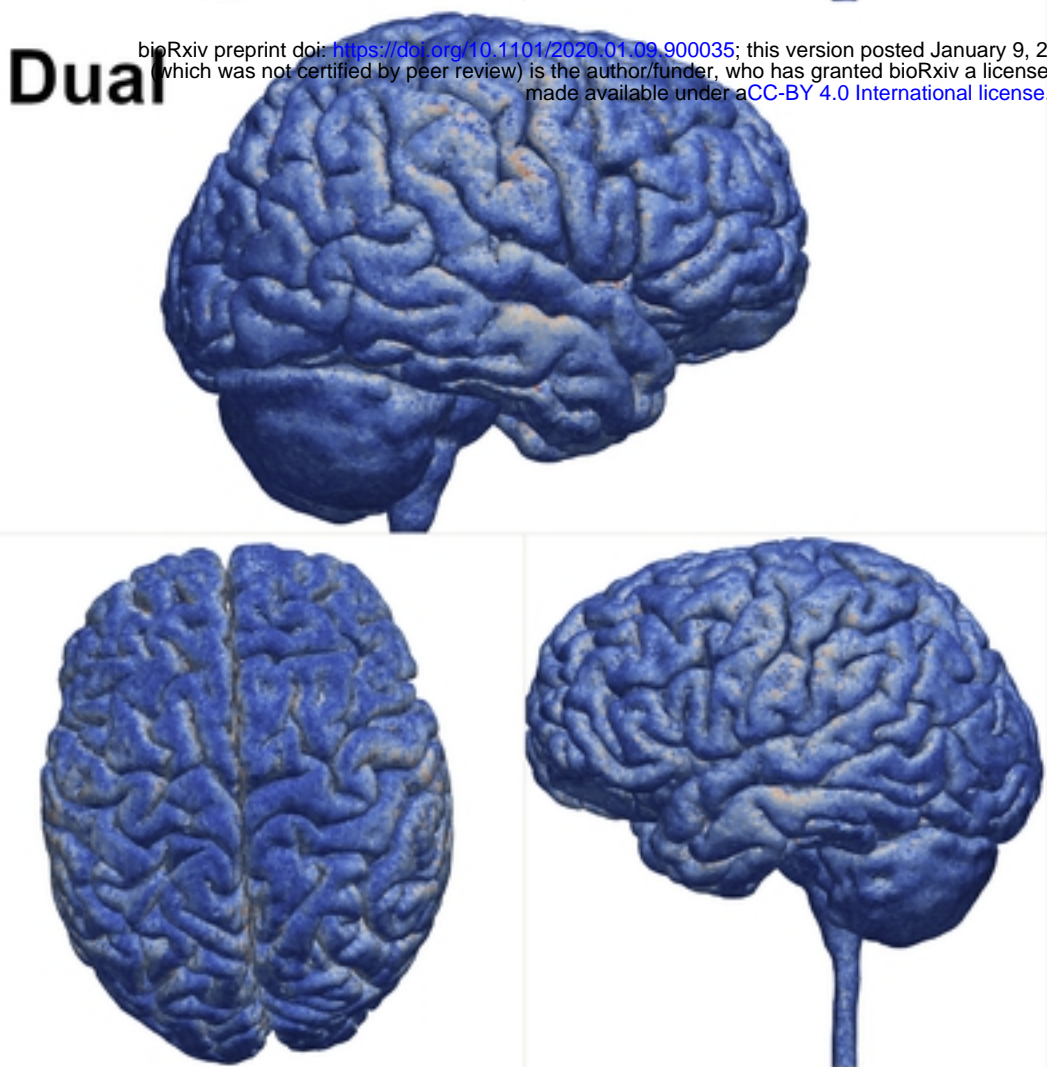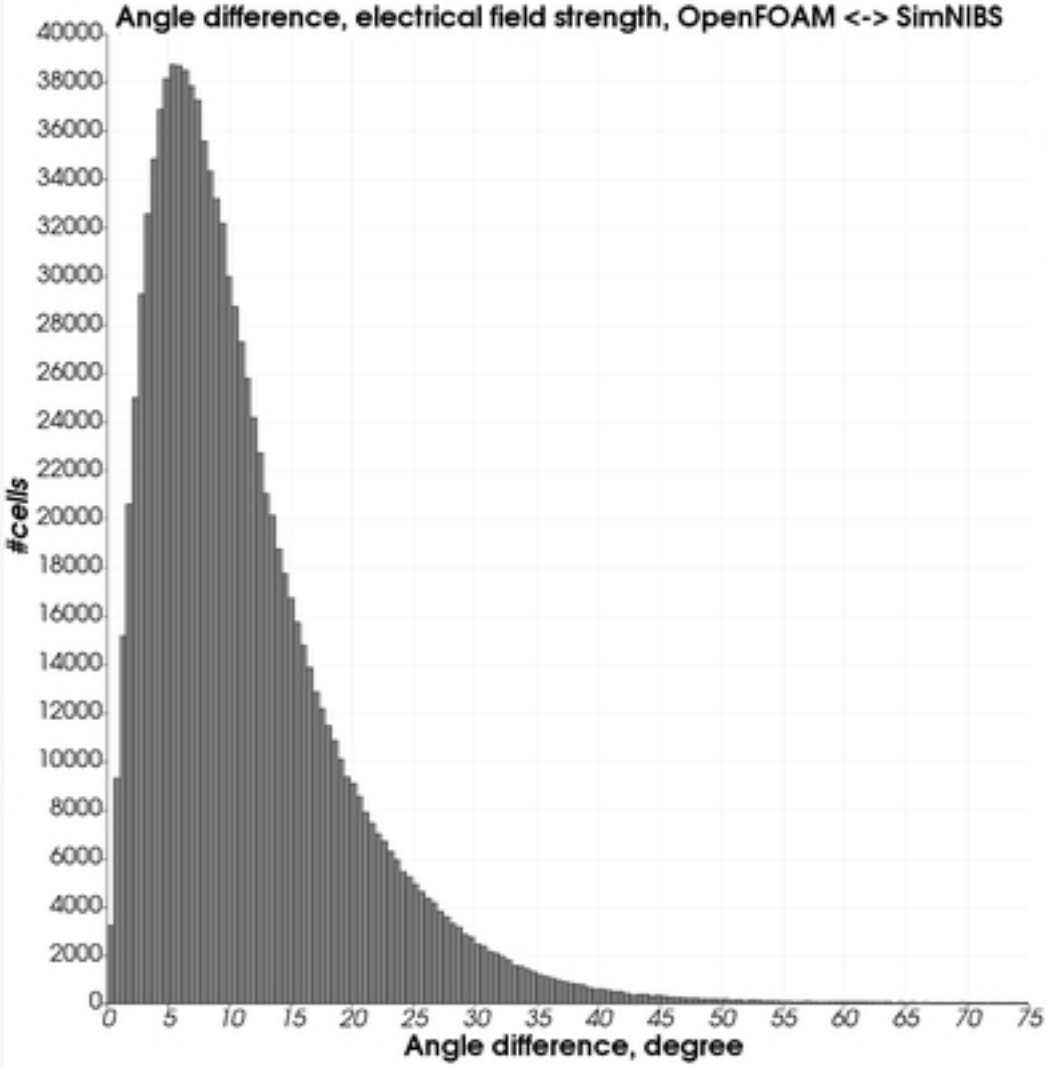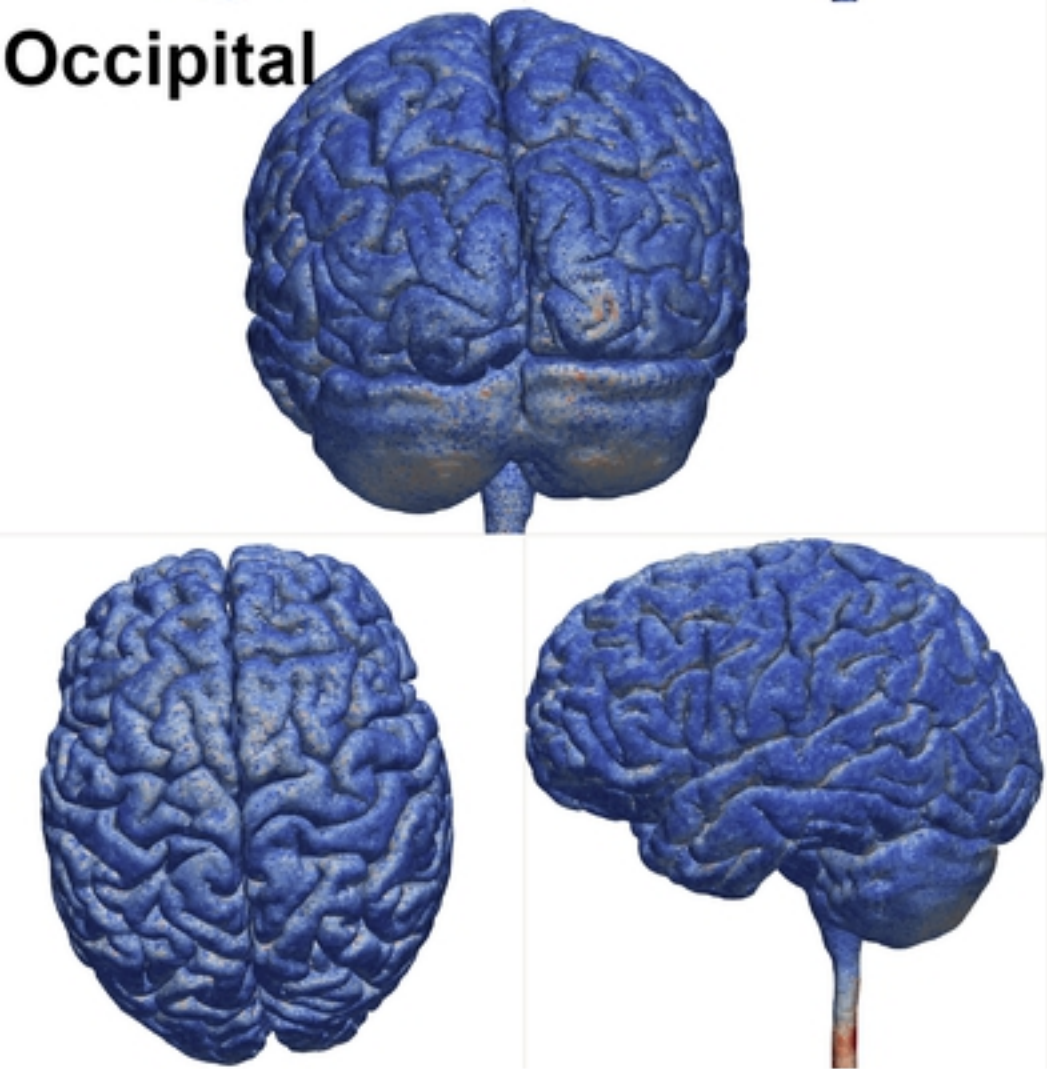
Anodal

Dual

Occipital

Figure 6

Figure 7

Anodal

Relative difference, %
-100 -80 -60 -40 -20 0 20 40 60 80 100

Relative Difference, electrical field strength, OpenFOAM <-> SimNIBS

Dual

Relative difference, electrical field strength, OpenFOAM <-> SimNIBS

Occipital

Relative Difference, electrical field strength, OpenFOAM <-> SimNIBS

Figure 8

Anodal

Angle Difference, degree

0.00 10 20 30 40 50 60 70.0

Angle difference, electrical field strength, OpenFOAM <-> SimNIBS

Dual

Angle difference, electrical field strength, OpenFOAM <-> SimNIBS

Occipital

Relative Difference, electrical field strength, OpenFOAM <-> SimNIBS
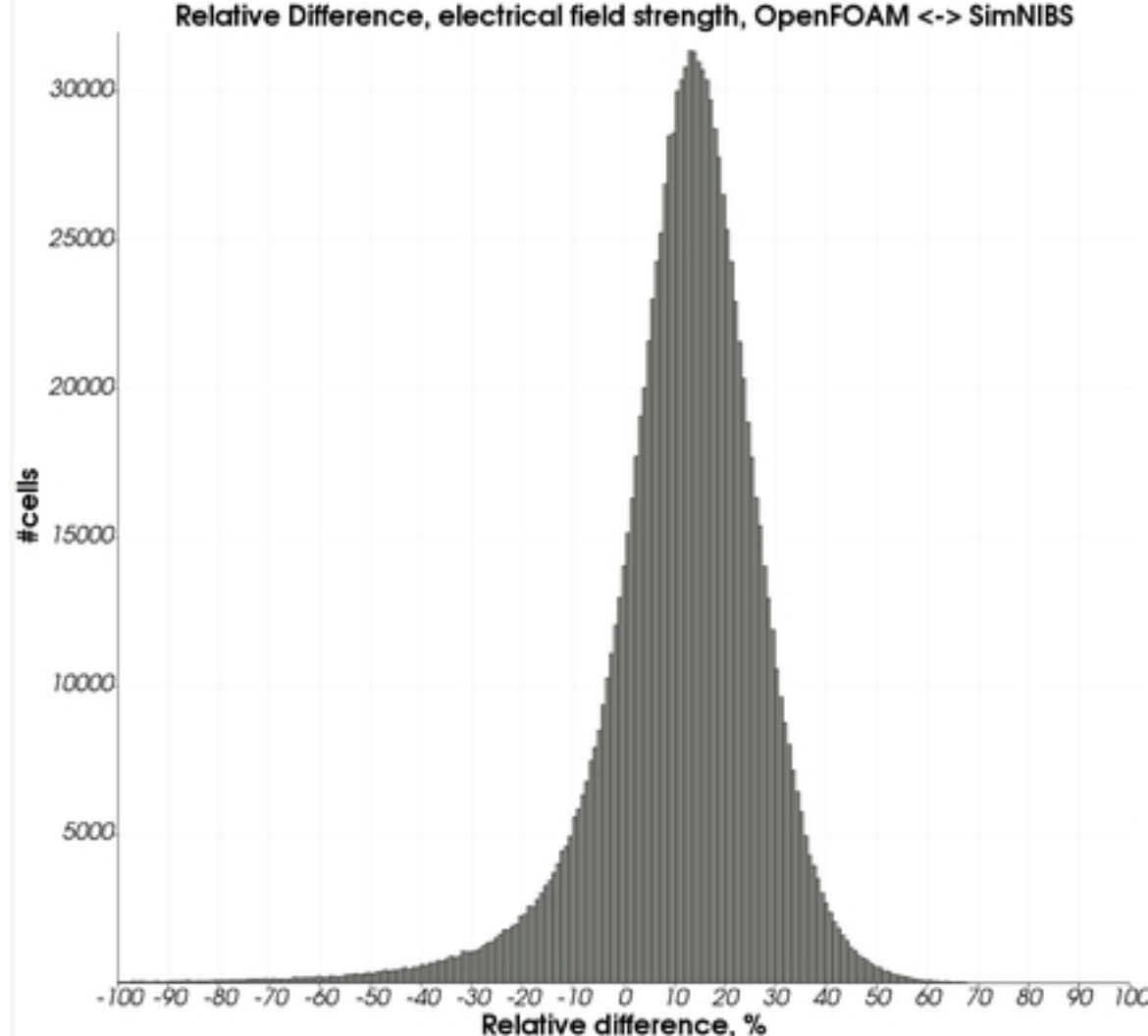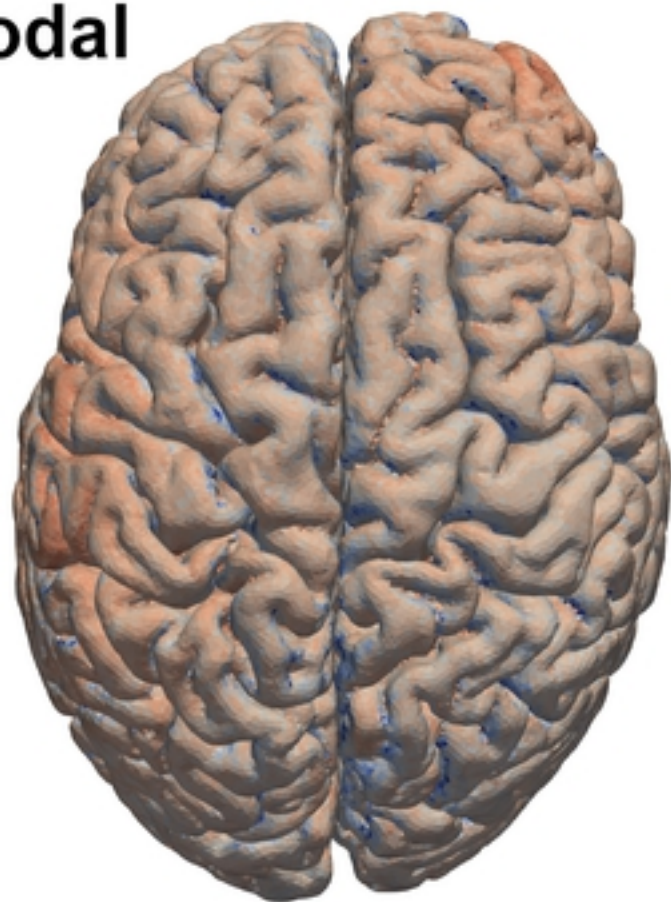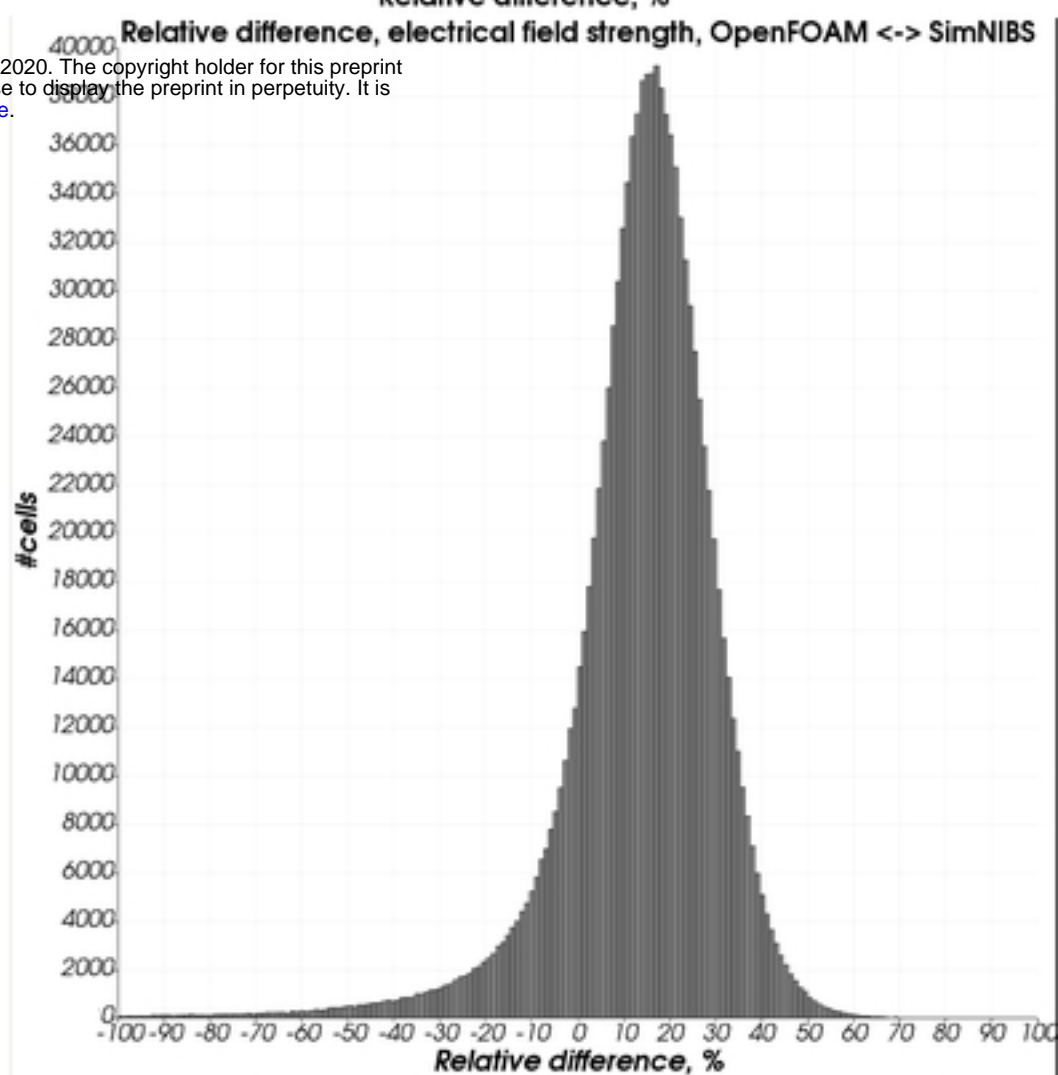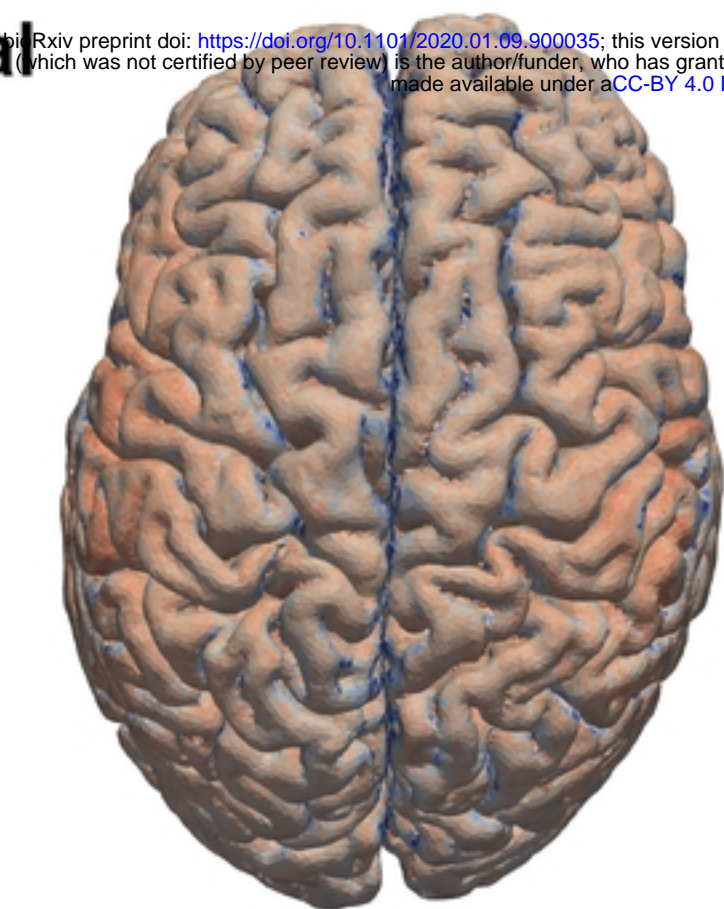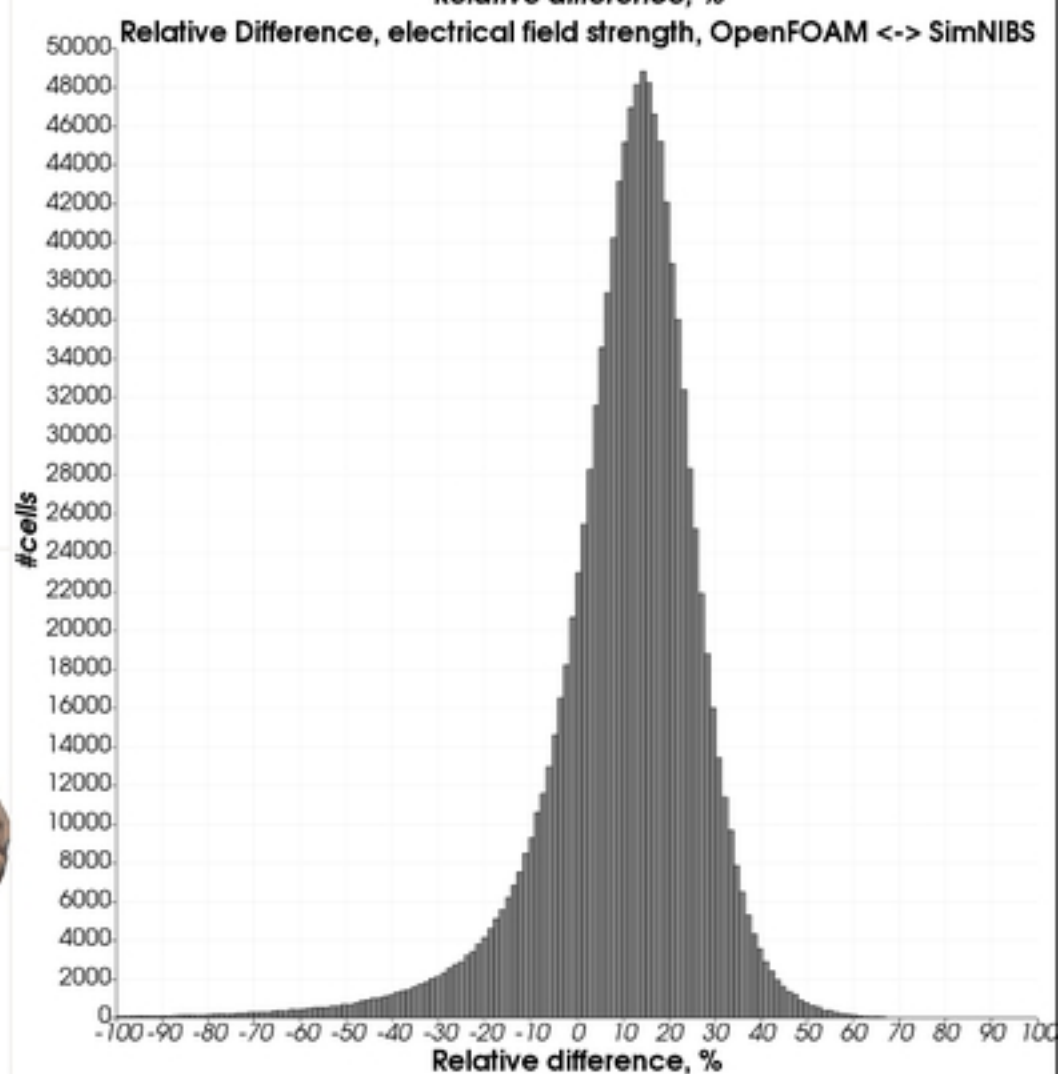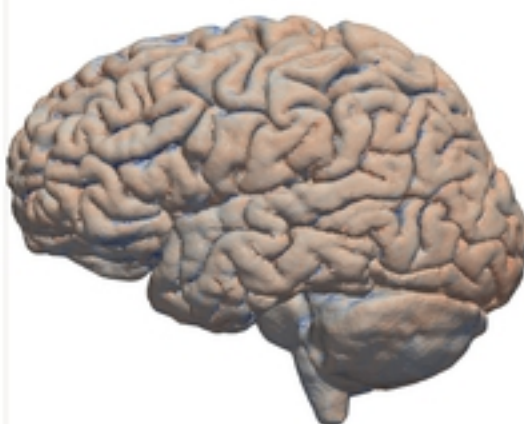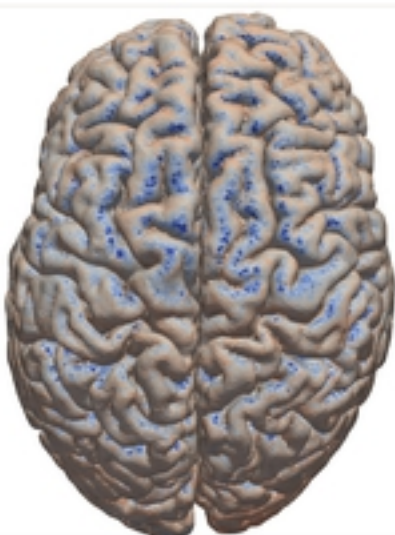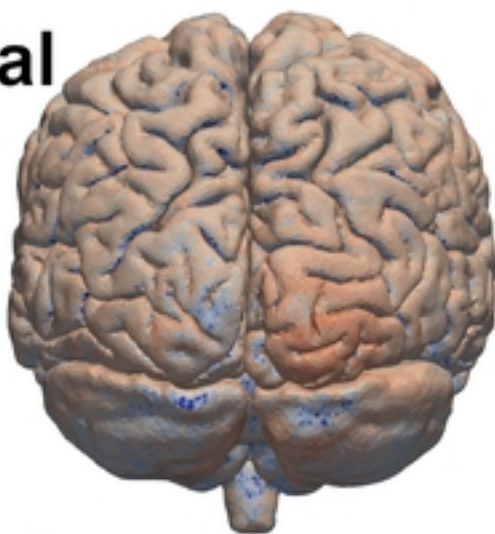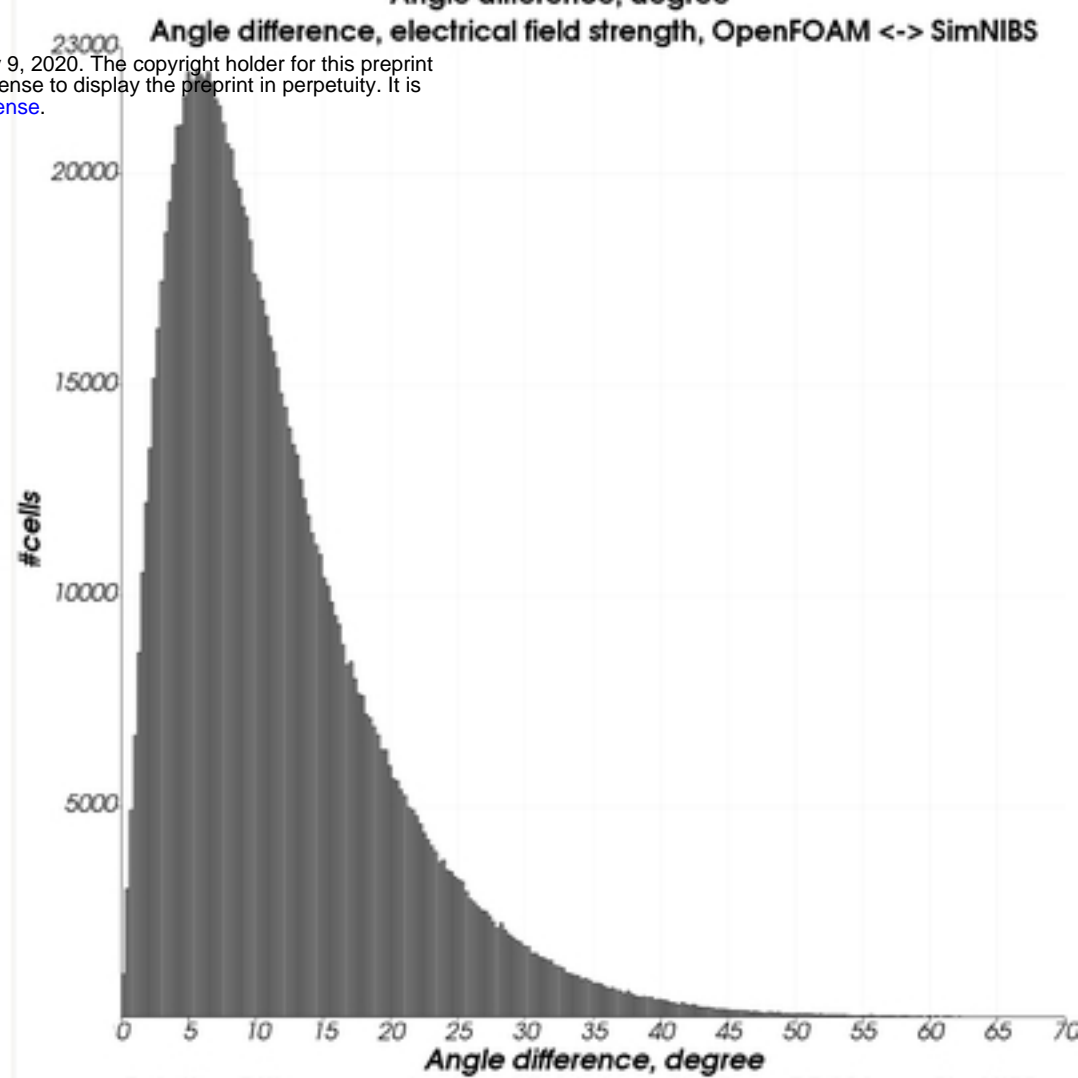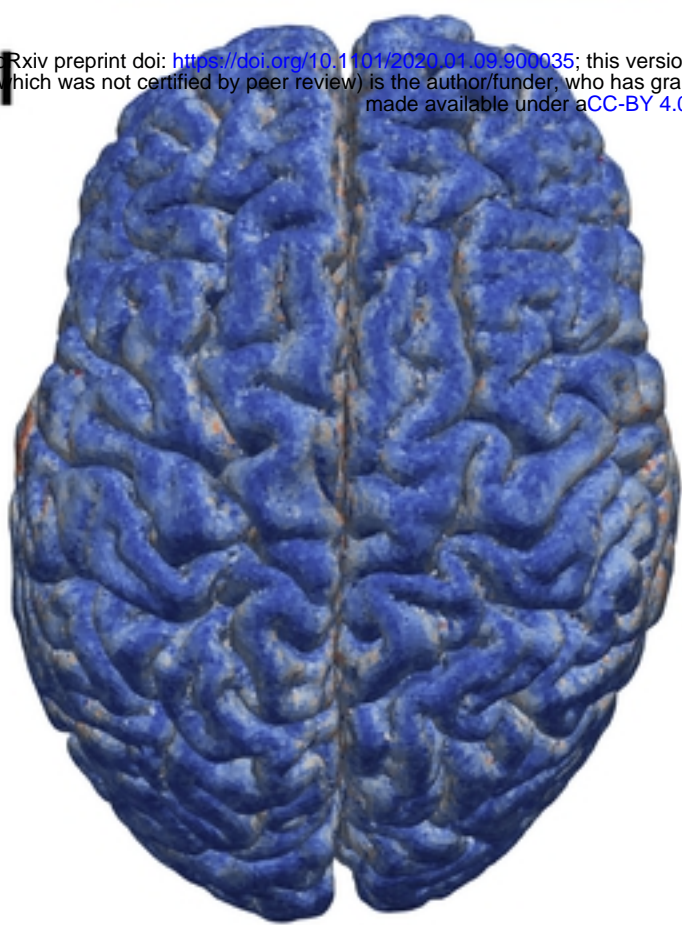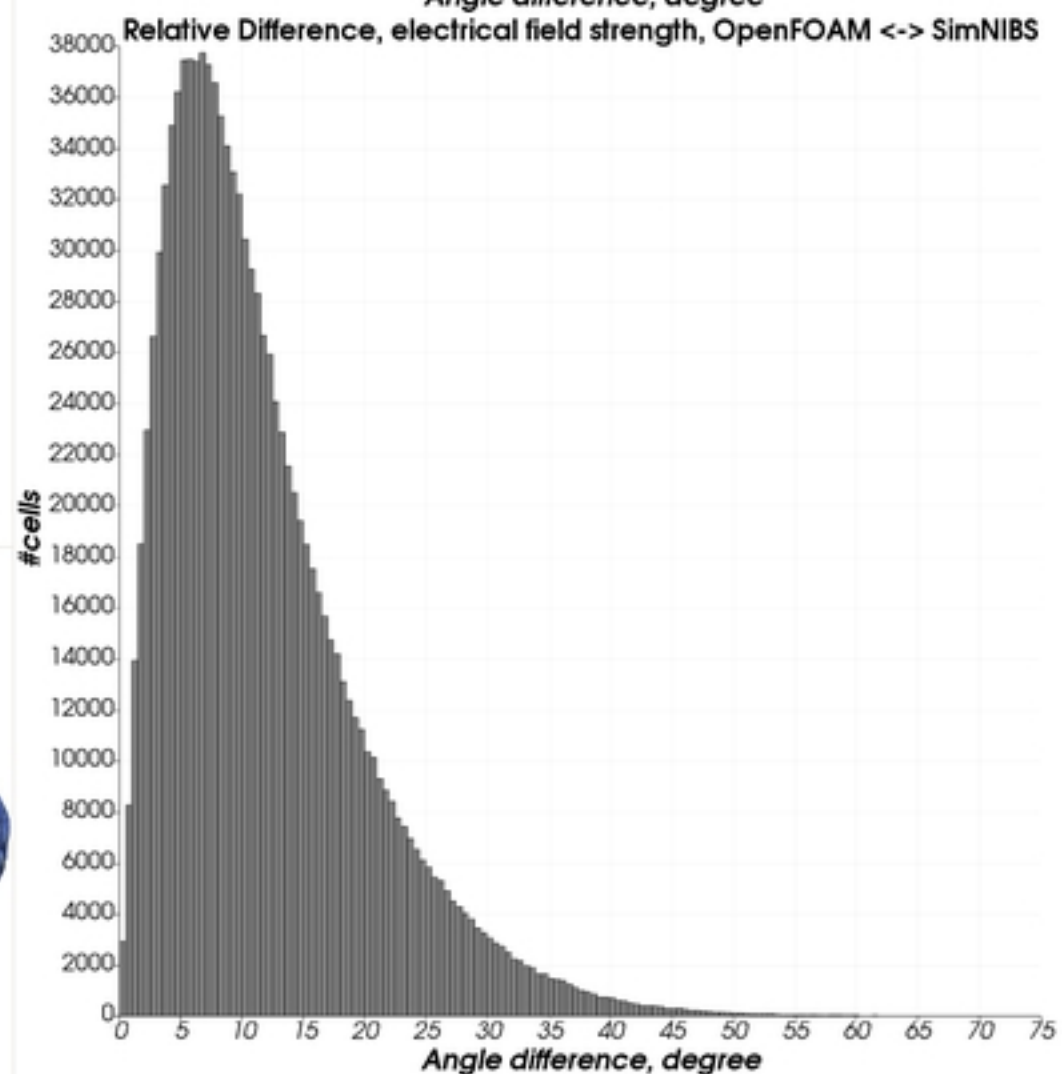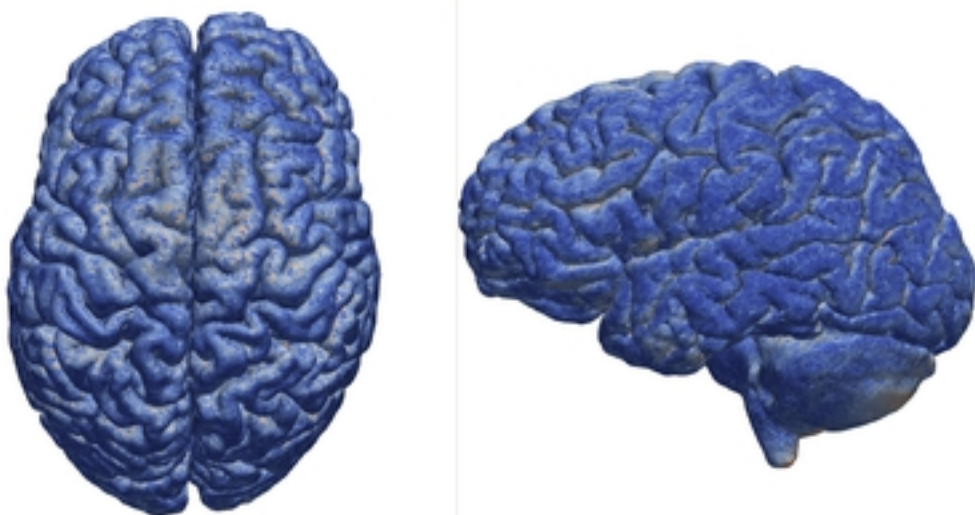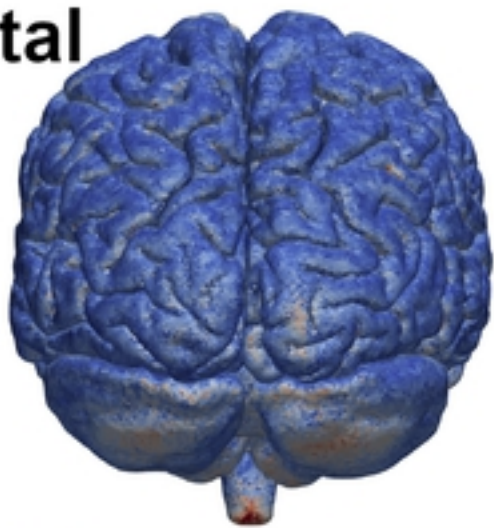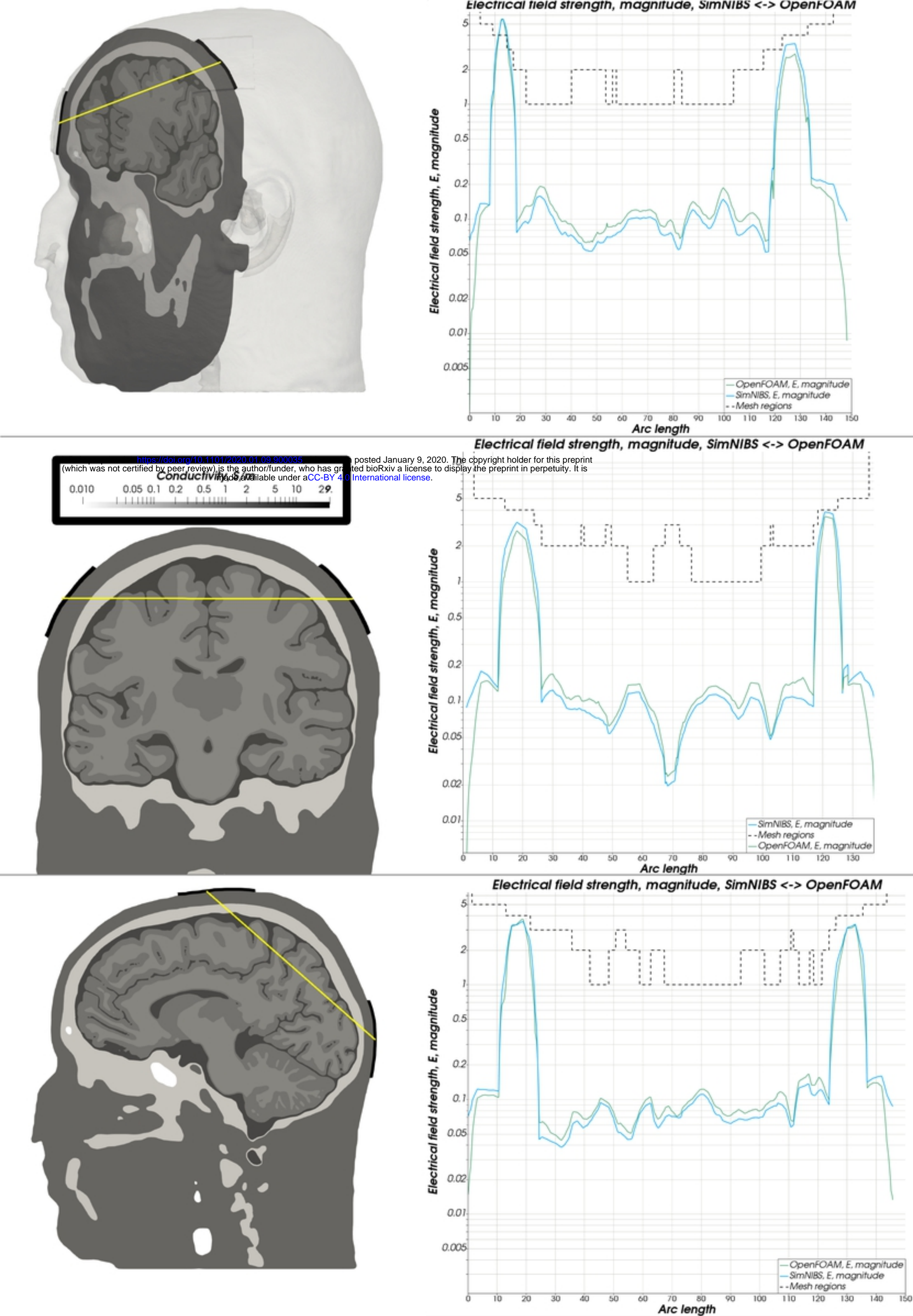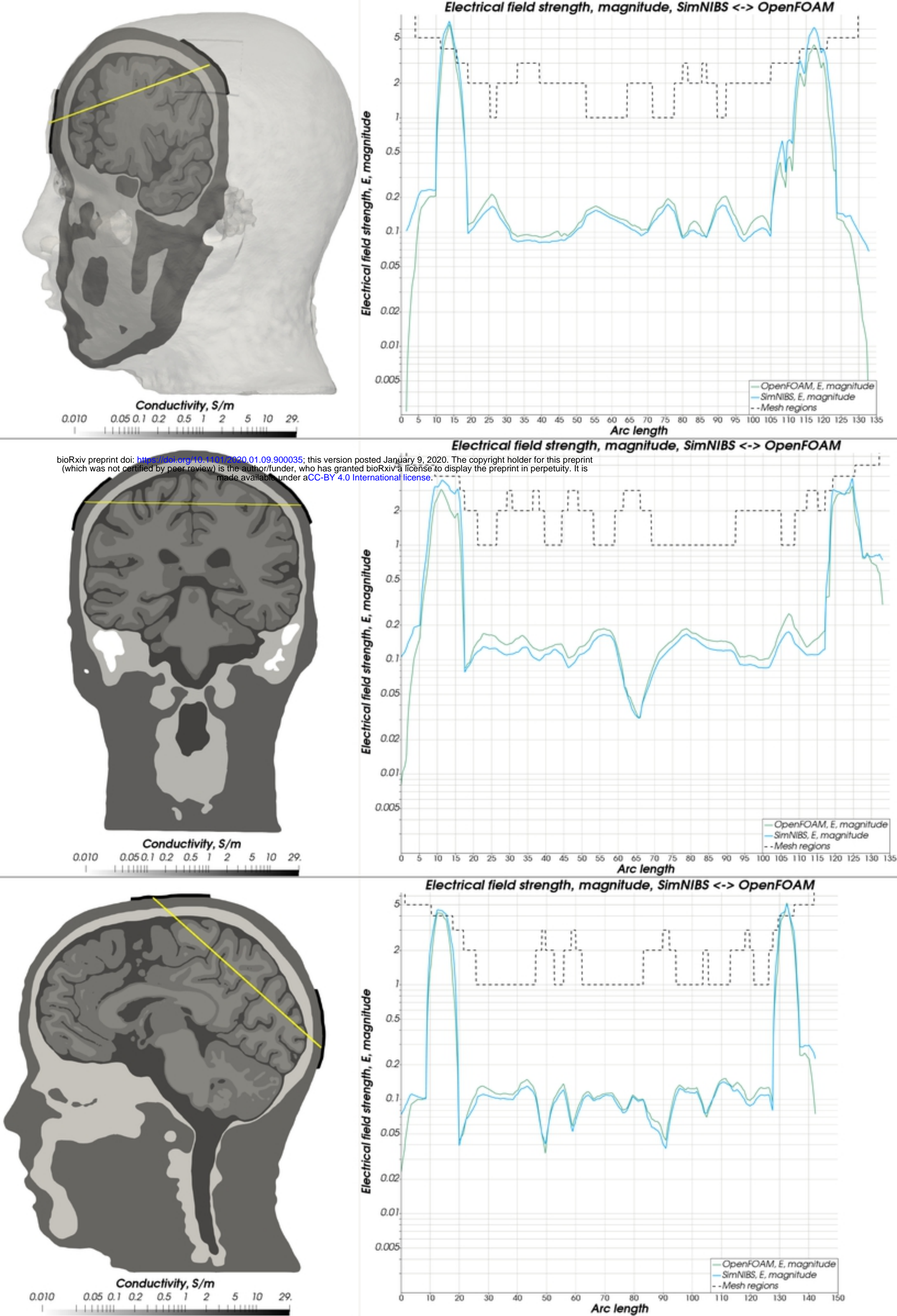
Figure 9

Figure 10

Figure 11

A) Head segmentation SimNIBS
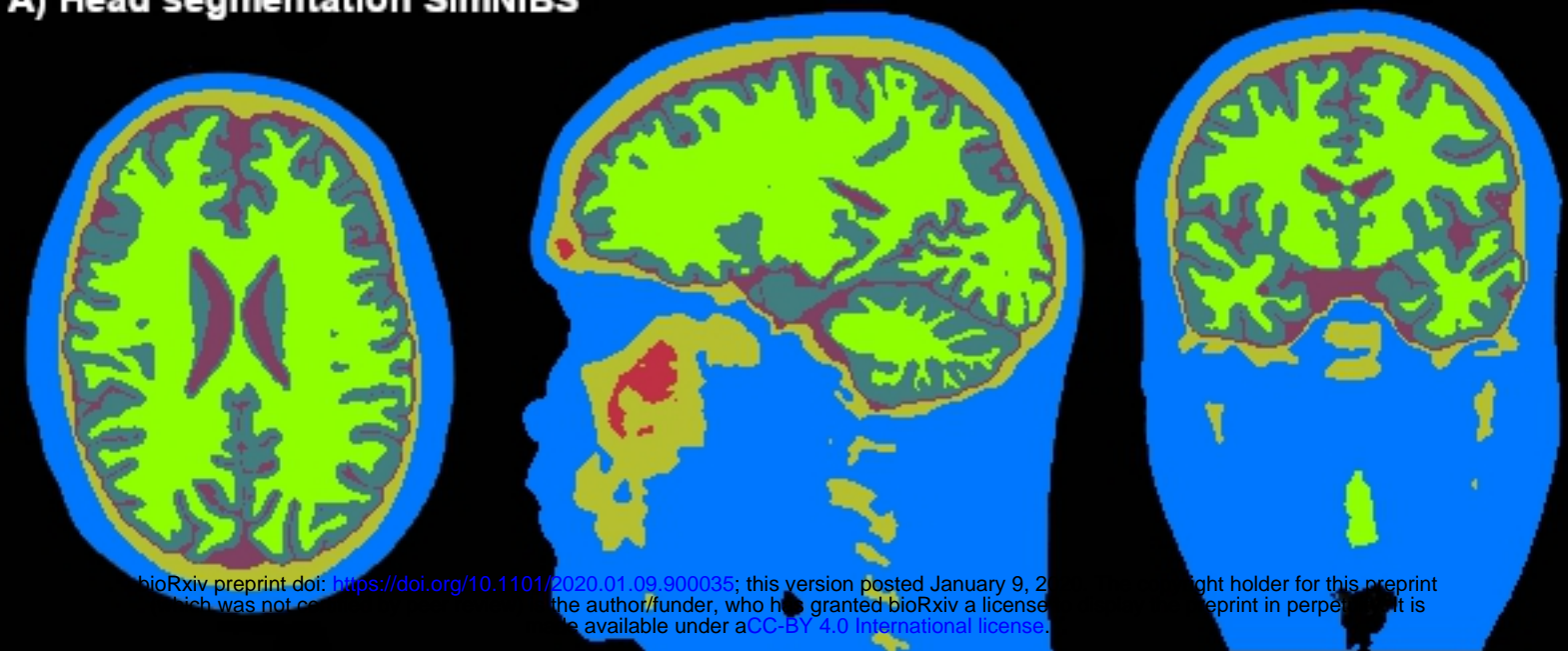
B) Original MR image

C) Our head segmentation
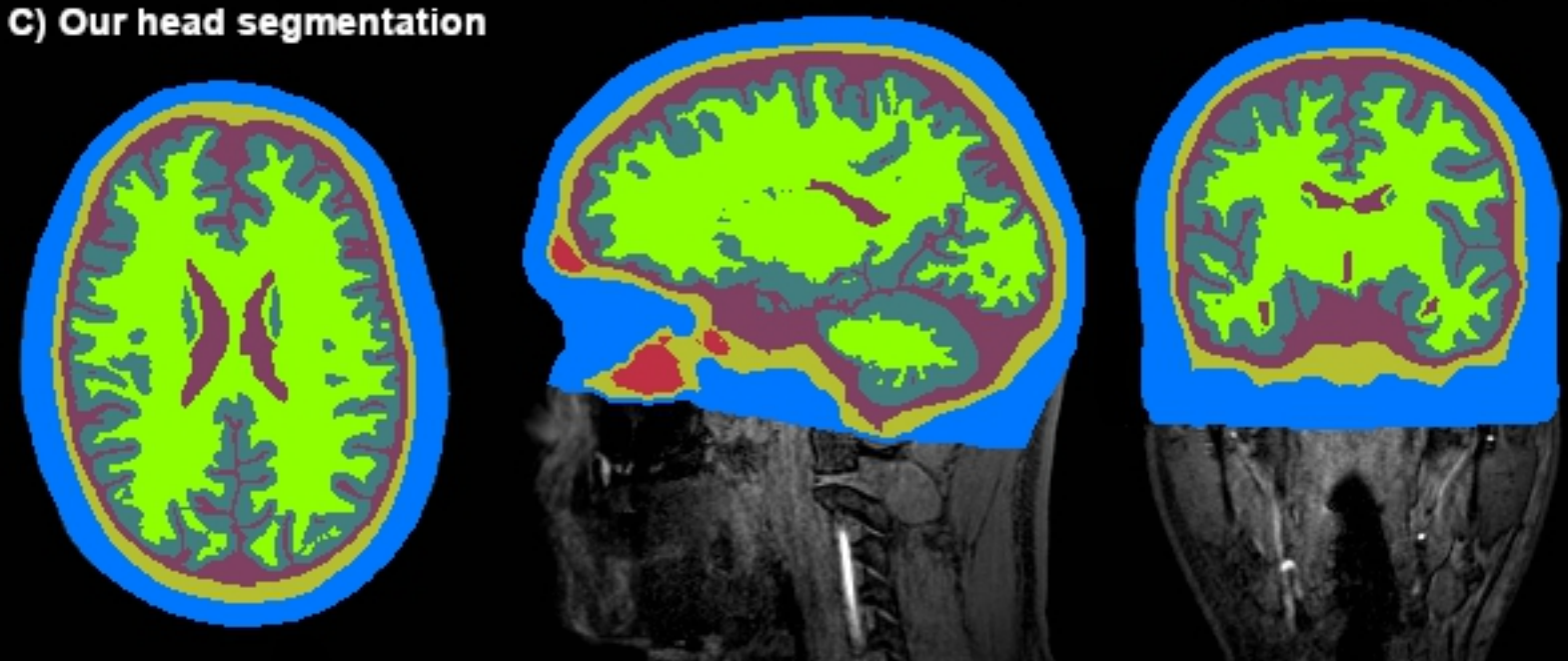
D) Electrical field (anodal electrode config.)
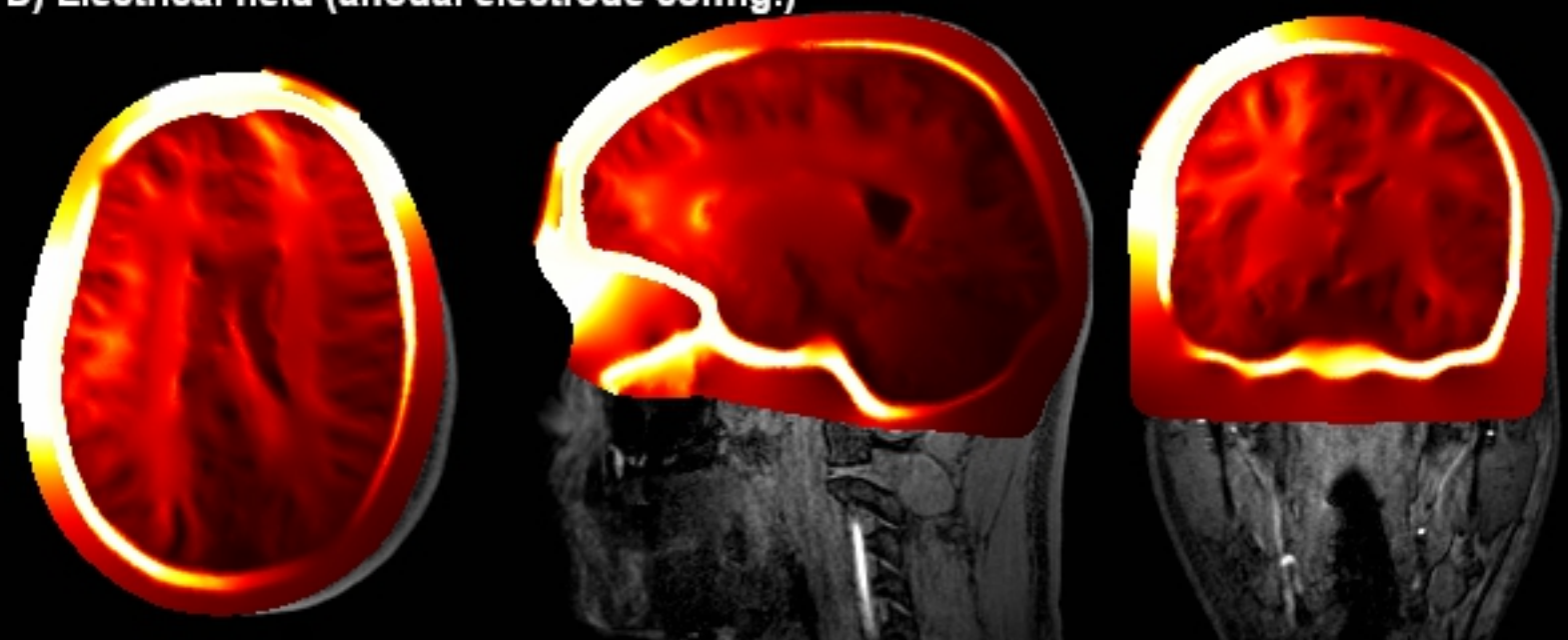
Figure 12
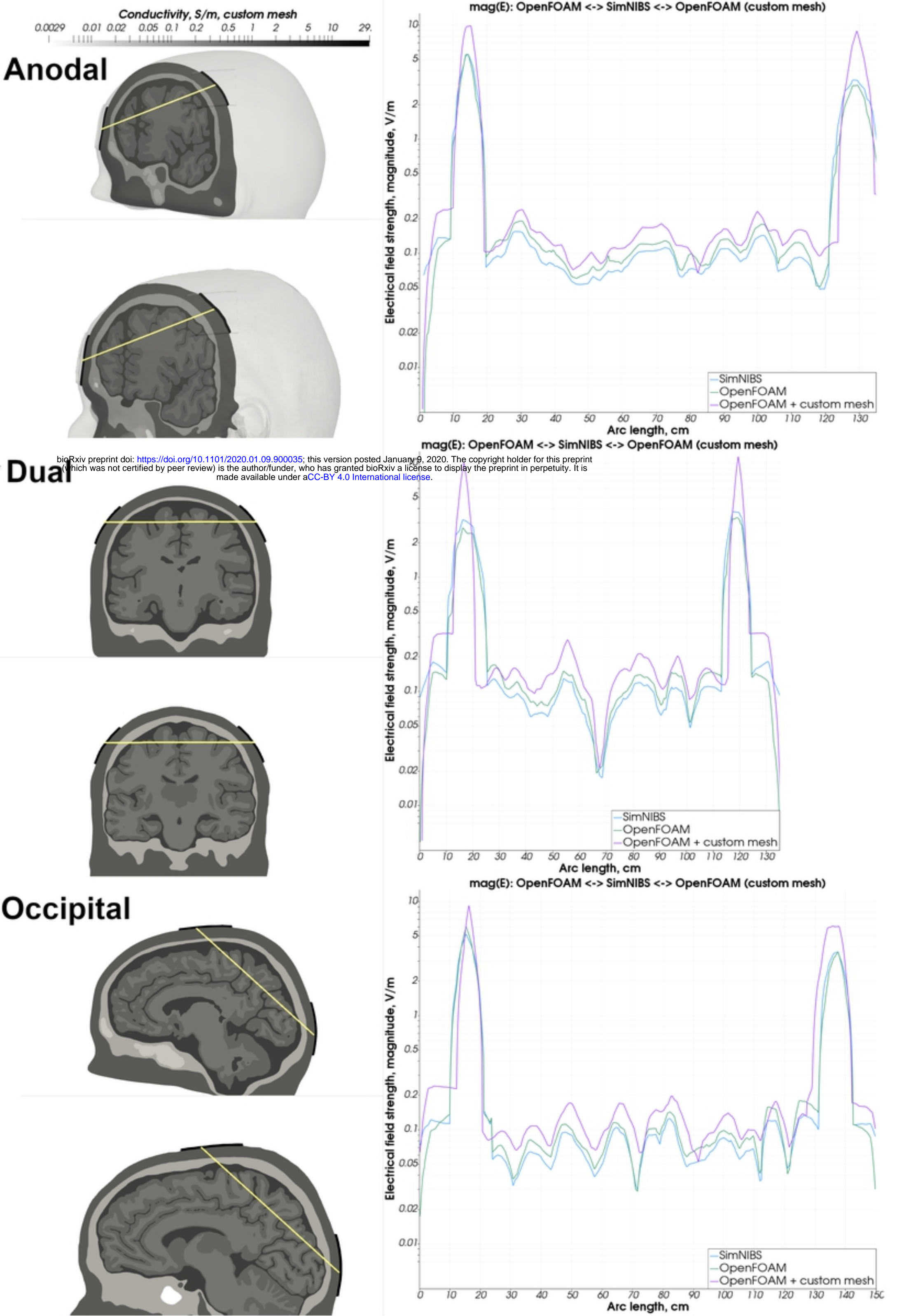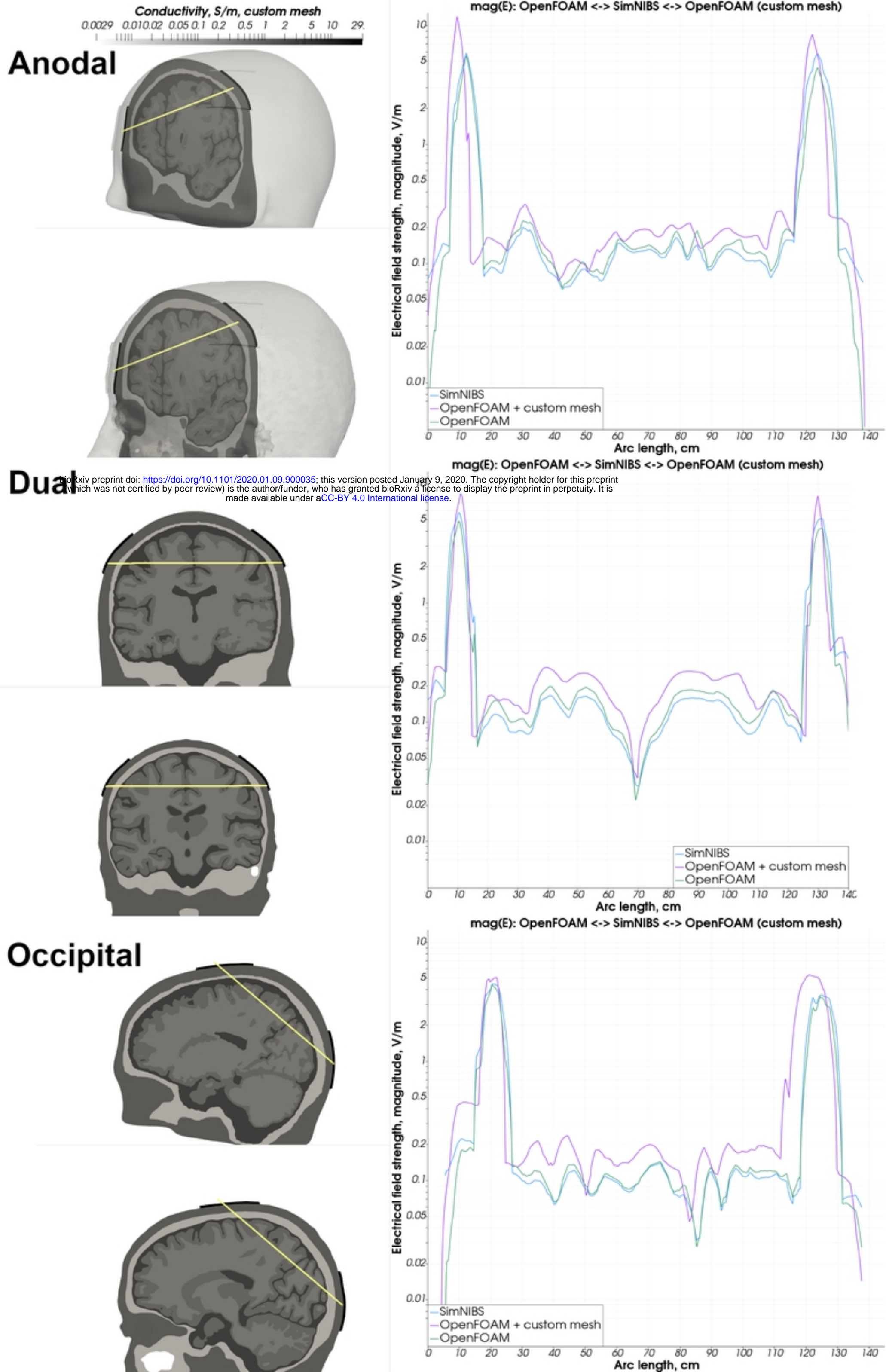
Figure 13
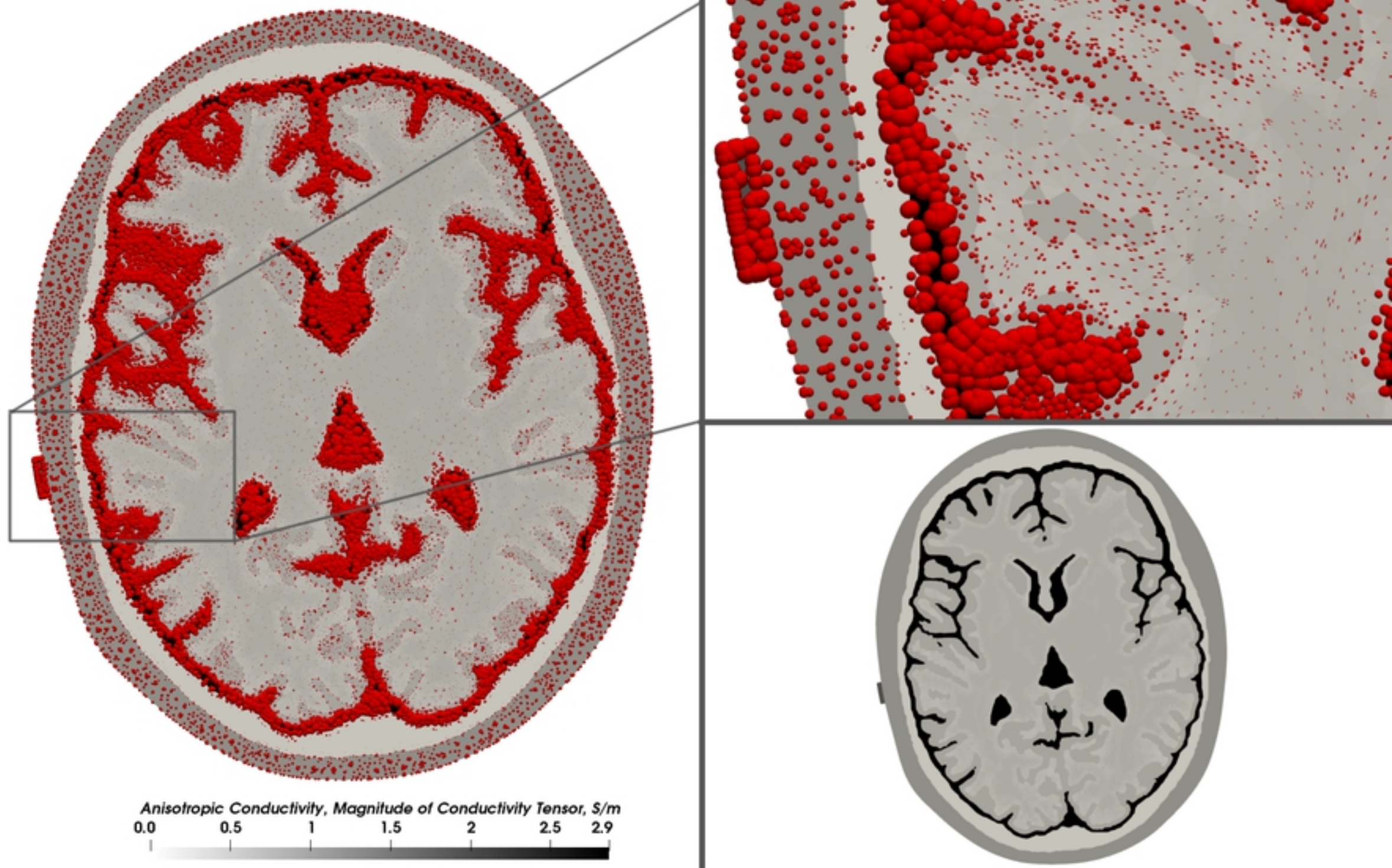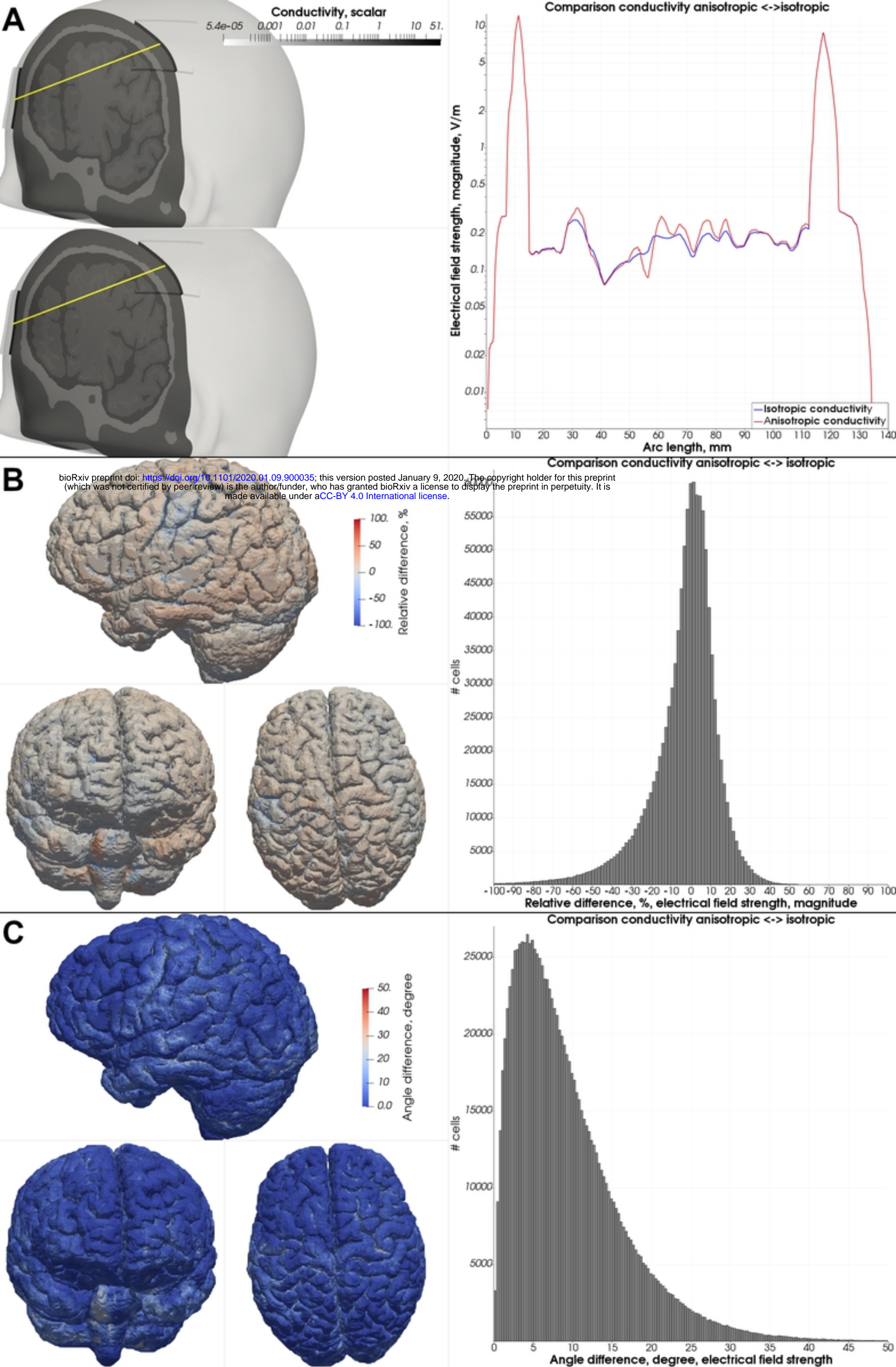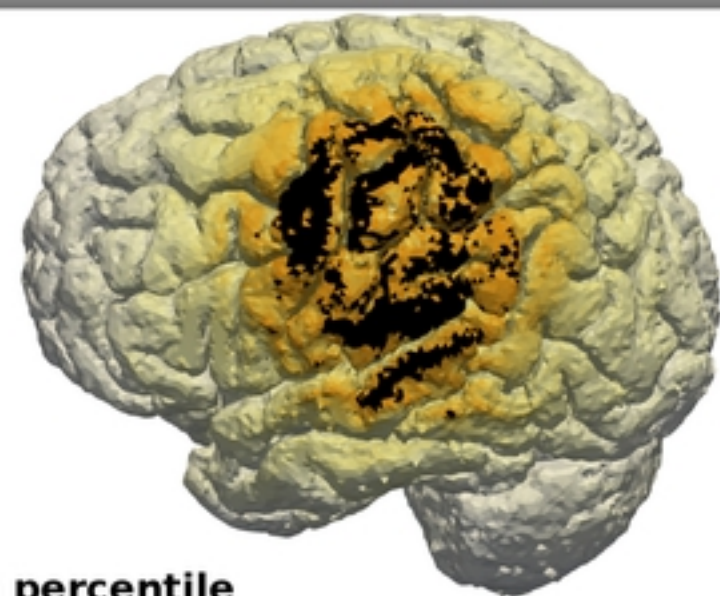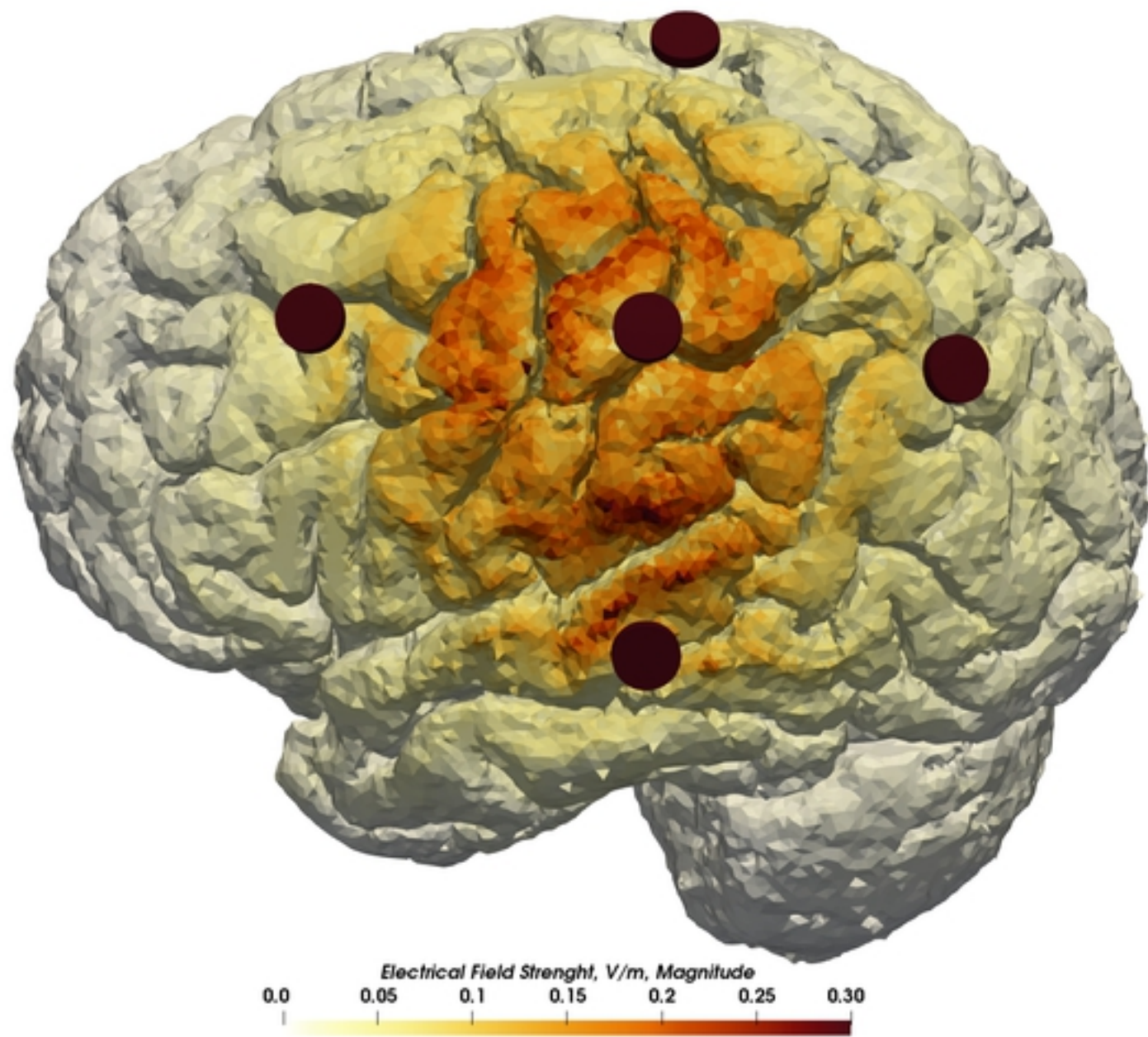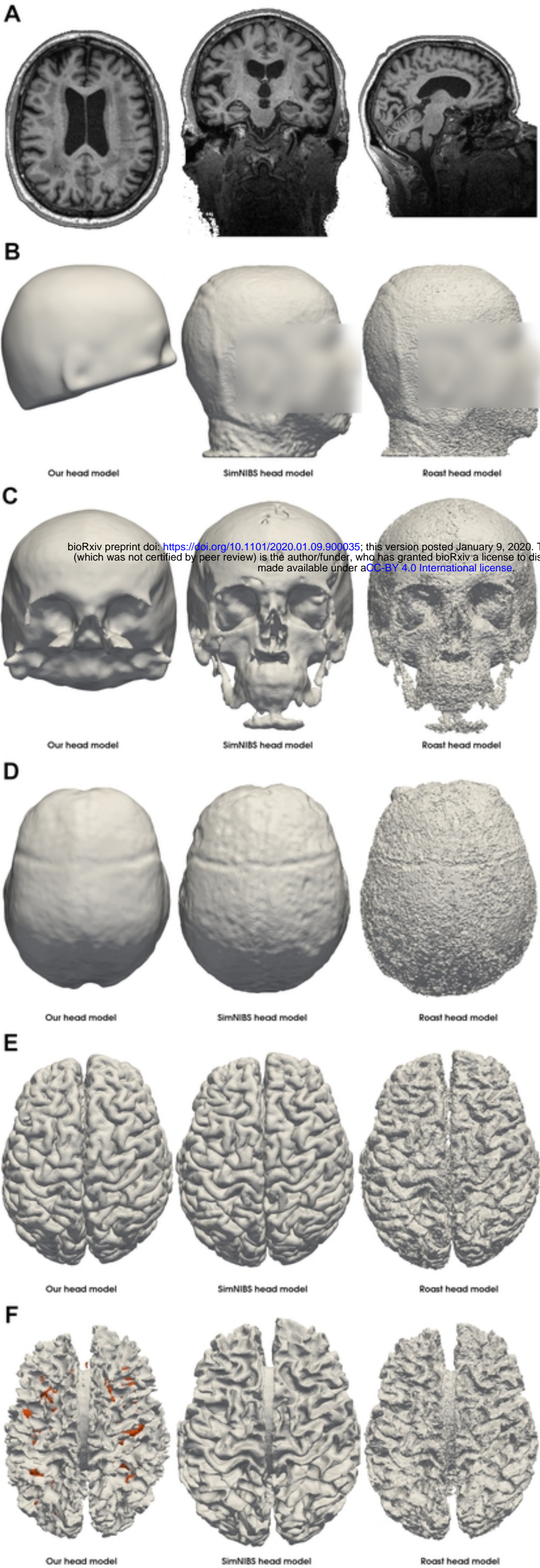
Figure 14

Anisotropic Conductivity, Magnitude of Conductivity Tensor, S/m
0.0   0.5   1   1.5   2   2.5   2.9

Figure 15

Figure 16

Figure 17

99th percentile

Electrical Field Strenght, V/m, Magnitude

0.0   0.05   0.1   0.15   0.2   0.25   0.30
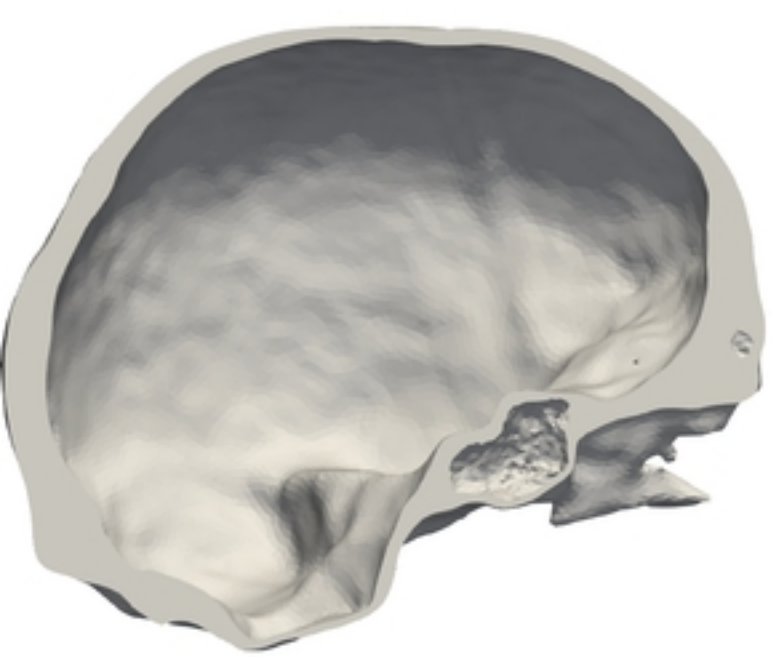
A

B

Our head model   SimNIBS head model   Roast head model

C

Our head model   SimNIBS head model   Roast head model

D

Our head model   SimNIBS head model   Roast head model

E

Our head model   SimNIBS head model   Roast head model
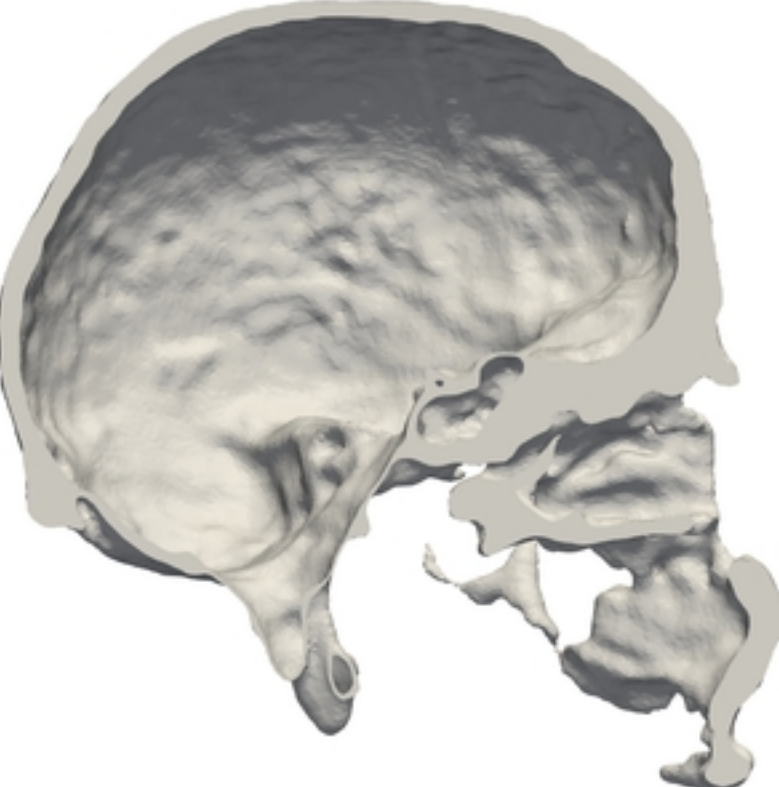
F

Our head model   SimNIBS head model   Roast head model

Figure 18

A
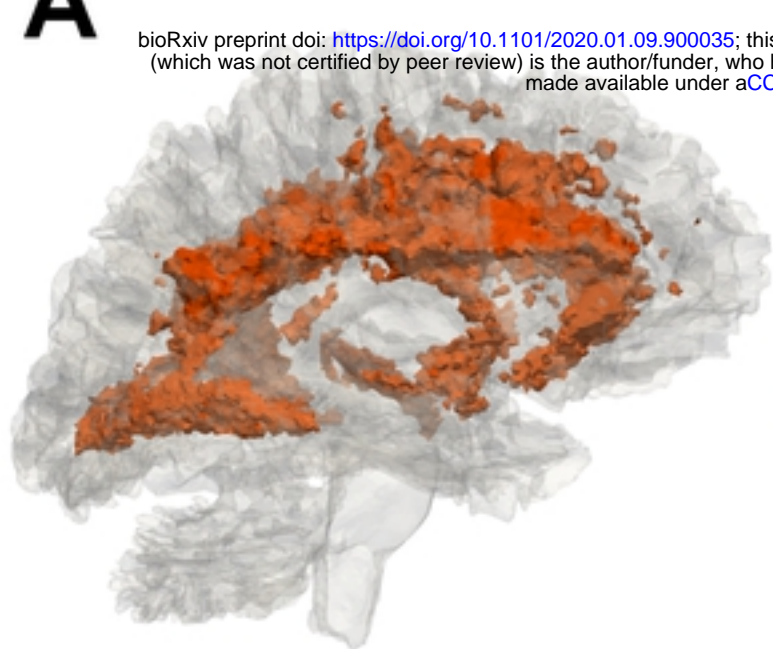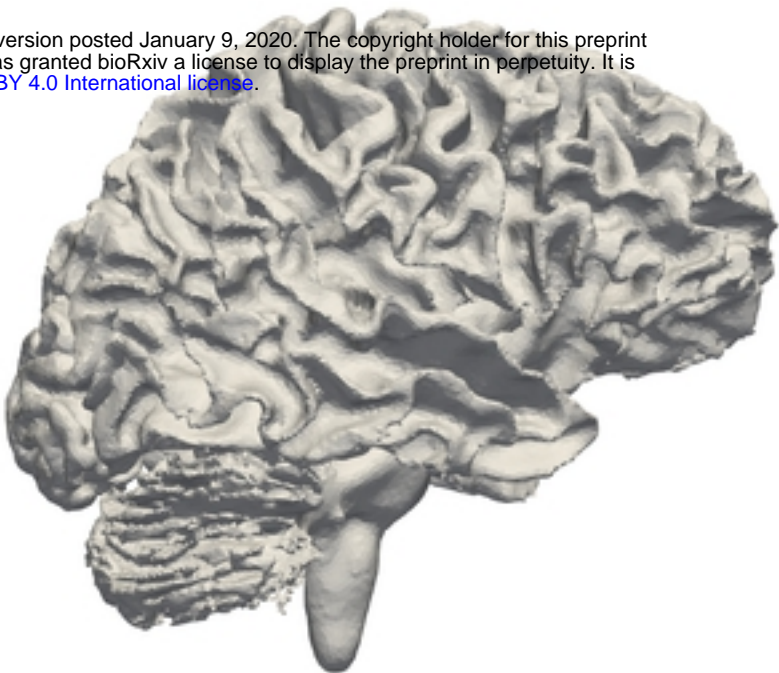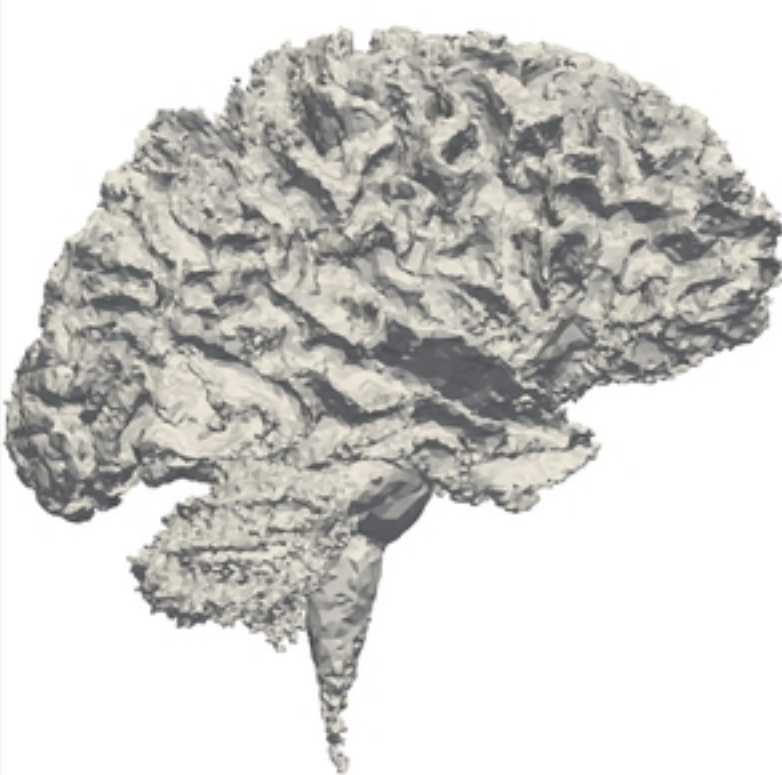
Our head model   SimNIBS head model   Roast head model
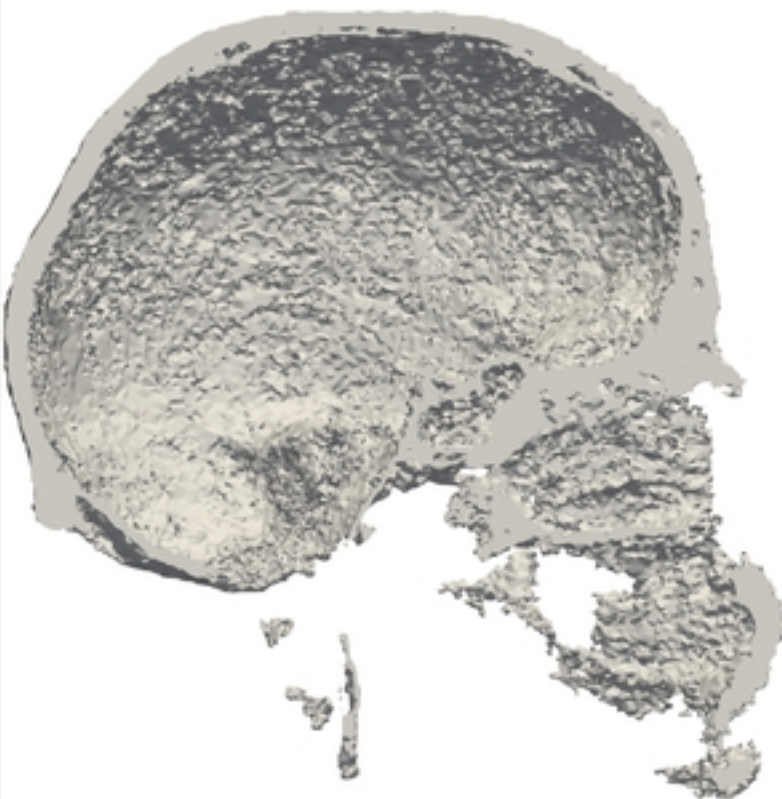
B

Our head model   SimNIBS head model   Roast head model

Figure 19

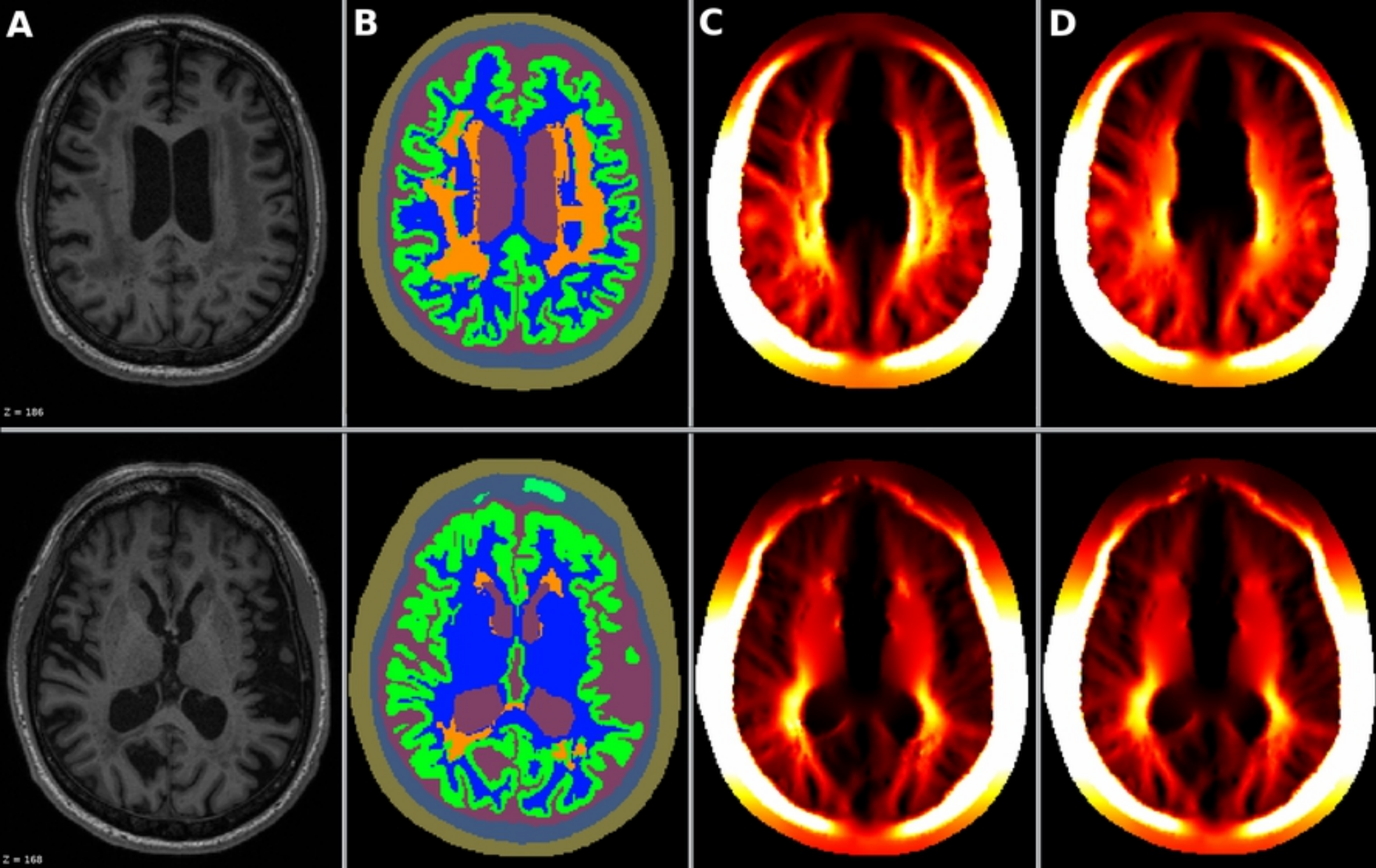Figure 20